Tampere University

Joona Leinonen

REAL-TIME ELECTRICAL EMULATION OF LI-ION BATTERY STORAGE USING POWER-HARDWARE-IN-THE-LOOP

Faculty of Computing and Electrical Engineering
Master's thesis
June 2019

ABSTRACT

JOONA LEINONEN: Real-time Electrical Emulation of Li-ion Battery Storage Using Power-Hardware-in-the-Loop
Tampere University
Master's Thesis, 55 pages, 3 Appendix pages
June 2019
Master's Degree Programme in Computing and Electrical Engineering
Major: Power Electronics
Examiner: Academy Research Fellow Tomi Roinila
Keywords: Li-ion battery, aging, impedance, pseudo-random binary sequence, emulation

Li-ion batteries have become increasingly important in several engineering fields of technology. The batteries play a crucial role, for example, in renewable energy applications in which battery storages are used to balance the power fluctuations caused by continuously varying weather conditions. Another good example is electric vehicles whose operation is most often dependent on Li-ion batteries.

The ever-increasing applications of Li-ion batteries have set new challenges in battery analysis. In order to know when the battery must be replaced and in which application it might still be utilized, knowing the age of the battery is crucial. The battery state of health (SoH) is used to estimate the aging and degradation of the battery. The SoH can be estimated by measuring the battery internal impedance since it is highly dependent on the aging processes.

Studying the battery aging is time-consuming because of the slow aging mechanisms and charging or discharging the battery to the desired operating state. This thesis studies methods for emulating the battery aging in real time using power-hardware-in-the-loop environment. The methods make it possible to analyze the SoH of Li-ion batteries within a short time without utilizing the actual aging process.

This thesis presents the modeling of Li-ion battery impedance and the implementation of battery emulation. The battery impedance model parameters are extracted from real data using a complex nonlinear least squares algorithm. Battery aging models are used to vary the battery SoH in real time. The operation of the emulation setup is verified by impedance measurements using wideband-identification techniques.

TIIVISTELMÄ

JOONA LEINONEN: Reaaliaikainen litiumioniakun sähköinen emulointi käyttäen PHIL-simulaatiota
Tampereen yliopisto
Diplomityö, 55 sivua, 3 liitesivua
Kesäkuu 2019
Sähkötekniikan diplomi-insinöörin koulutusohjelma
Pääaine: Tehoelektroniikka
Tarkastaja: Akatemiatutkija Tomi Roinila
Avainsanat: litiumiomiakku, ikääntyminen, impedanssi, pseudosatunnainen binäärisekvenssi, emulaatio

Uusiutuvan energian ja sähköautojen määrä on lisääntynyt runsaasti viimeisten vuosien aikana. Sähköautot käyttävät litiumioniakkuja energiavarastoinaan, ja uusiutuvien energialähteiden yhteyteen voidaan liittää energiavarastoja vaihtelevien sääolosuhteiden aiheuttaman voimalan tehon heilahtelun tasaamiseksi.

Litiumioniakkujen määrän kasvu on aiheuttanut haasteen akkujen kierrättämiselle ja akkujen iän estimoinnille. Jotta tiedettäisiin milloin akku pitää vaihtaa ja millaiseen sovellukseen sitä voitaisiin vielä hyödyntää, on akun iän tunteminen erittäin tärkeää. Akun kuntotilaa voidaan arvioida sen sisäisellä impedanssilla, joka muuttuu selkeästi akun ikääntyessä.

Akun ikääntymisen tutkiminen on hidasta sillä ikääntymismekanismit ovat hitaita ja akkua joudutaan lataamaan ja purkamaan aina mittausten välillä. Tässä työssä akkua emuloidaan reaaliajassa, jolloin sen ikää voidaan muuttaa nopeasti.

Tämä diplomityö esittelee litiumioniakun impedanssin mallintamista sekä sen ikää emuloivan laboratorioympäristön toteuttamisen. Akun impedanssin mallin parametrit estimoidaan oikeasta datasta käyttäen kompleksista epälineaarista pienimmän neliösumman menetelmää. Akun ikäätymismalleja käytetään akun kuntotilan muuttamiseen reaaliajassa. Laboratorioympäristön toiminta varmennetaan emuloidun akun impedanssin mittaamisella käyttäen laajakaistaisiin herätteisiin perustuvaa identifiointityökalua.

PREFACE

This thesis was accomplished in the laboratory of Electrical Energy Engineering at Tampere University. I would like to thank the new university and the department for giving me this opportunity to finish my studies.

Thanks to my examiner Dr. Tomi Roinila and ex-examiner Dr. Tuomas Messo for giving me this extremely interesting topic for my Master of science thesis, and all the guidance during the whole research process. Also thanks to my colleague Jussi Sihvo for his expertise in the field of batteries, and for the valuable comments during the writing process.

I would also like to thank my beloved fiancée for all the support and encouragement, which guided my way towards the Master of science. I thank my family for supporting me during all the years of studying and giving me the opportunity to educate myself even this far.

Last but definitely not least, I would like to thank all my colleagues for the all-around help during the work and for keeping up a top-notch working atmosphere in the office and around the ping-pong table.

Tampere, 29th June 2019

Joona Leinonen

CONTENTS

LIST OF FIGURES

ABBREVIATIONS AND SYMBOLS

ABBREVIATIONS

BoL	Beginning of Life
CPE	Constant phase element
DC	Direct current
DL	Diffusion layer
DoD	Depth-of-discharge
EC	Electrolytic cell
EEC	Equivalent electrical circuit
EIS	Electrochemical impedance spectroscopy
EoL	End of Life
EV	Electric vehicle
FFT	Fast fourier transform
FRF	Frequency response function
LTI	Linear time-invariant
MLBS	Maximum length binary sequence
OCV	Open Circuit Voltage
PHIL	Power Hardware-In-the-Loop
PRBS	Pseudo-random binary sequence
SEI	Solid electrolyte interface
SNR	Signal-to-noise ratio
SoC	State of charge
SoH	State of health

Symbols

A	Amplitude
A	Cross-sectional area of electrolyte
A	Exponential zone amplitude
α	Reaction order
B	Exponential zone time constant inverse
C	Capacitance
$C_{A...E}$	Approximated capacitances of ZARC element
C_D	Diffusion capacitance

C_{dl}	Double-layer capacitance
d	Depression factor
e	Electron
$e(t)$	White noise in system input
E_0	Constant voltage source
f	Frequency
f_{gen}	PRBS generation frequency
f_s	Frequency resolution
F	Faraday's constant
$g(t)$	Impulse response function in time domain
$G(j\omega)$	System transfer function frequency response
i_{emu}	Output current of battery emulator
i_{meas}	Measured current
i_{ref}	Current reference for dSPACE
I	Current
I_0	Exchange current
$I(j\omega)$	Current frequency response
κ	Conductvity
K	Polarization coefficient
$K_{1...4}$	Fitting constants
l	Length
L	Inductance
L_s	Series inductance
M	Metal
n	Number of shift registers
nc	Number of cycles
η	Over potential
N	Length of PRBS
Q	Generalized capacitance
Q	Nominal capacity of battery
Q_a	Available charge of battery
$r(t)$	White noise in system output
R	Gas constant
R	Resistance
$R_{A...E}$	Approximated resistances of ZARC element
R_{ct}	Charge transfer resistance
R_D	Diffusion resistance

R_{el}	Resistance of electrolyte
R_s	Series resistance
$R_{s,inc}(t)$	Series resistance increase as a function of time
s	Laplace variable
SoC_{init}	Initial state of charge
t	Time
T	Temperature
$U(j\omega)$	Voltage frequency response
V	Voltage
V_{Batt}	Terminal voltage of battery
V_{emu}	Output voltage of battery emulator
V_{meas}	Measured battery emulator voltage
V_{OC}	Open circuit voltage of battery
V_{ref}	Reference voltage for battery emulator
W	Warburg coefficient
ω	Angular frequency
$\omega_{0_{ZARC}}$	Characteristic frequency of ZARC element
x	Number of electrons
$x(t)$	System input signal in time domain
$x_e(t)$	Measured system input signal
X	Reducing agent
$X(j\omega)$	System input signal frequency response
$y(k)$	Cell terminal voltage in discrete time
$y(t)$	System output response in time domain
$y_r(t)$	Measured system output response
$Y(j\omega)$	System output signal frequency response
Z_{CPE}	Impedance of constant phase element
$Z(j\omega)$	Impedance frequency response
Z_W	Warburg impedance
Z_{ZARC}	Impedance of ZARC element

1. INTRODUCTION

Global warming is nowadays widely known caused by man-made greenhouse gas emissions. Awareness that polluting the atmosphere with these gasses increase global temperature rise and resulting in dramatic climate changes, has increased the urgency for replacing the fossil fuels with clean energy sources. According to [1], 50% of the total world energy use could be covered with renewable energy by 2050. However, renewable energy sources such as wind and photovoltaic plants are highly dependent on weather conditions and day cycle. In order to balance the energy demand in the grid, the produced energy has to be stored for later use. The electrical energy storage system can be connected alongside the renewable energy source to balance the power mismatch in the grid.

Many energy storage systems have been researched in recent years but the most promising are battery storages and especially lithium-ion batteries. Lithium-ion batteries have many advantageous characteristics such as high energy and power density, high efficiency and relatively long lifetime, compared to other battery chemistries. [2–4] The high energy density of Li-ion batteries can be seen as a large area in Fig. 1.1, where power and discharge times are shown for various energy storage technologies. As a drawback, Li-ion batteries are still an expensive energy storage component with an uncertain lifetime.

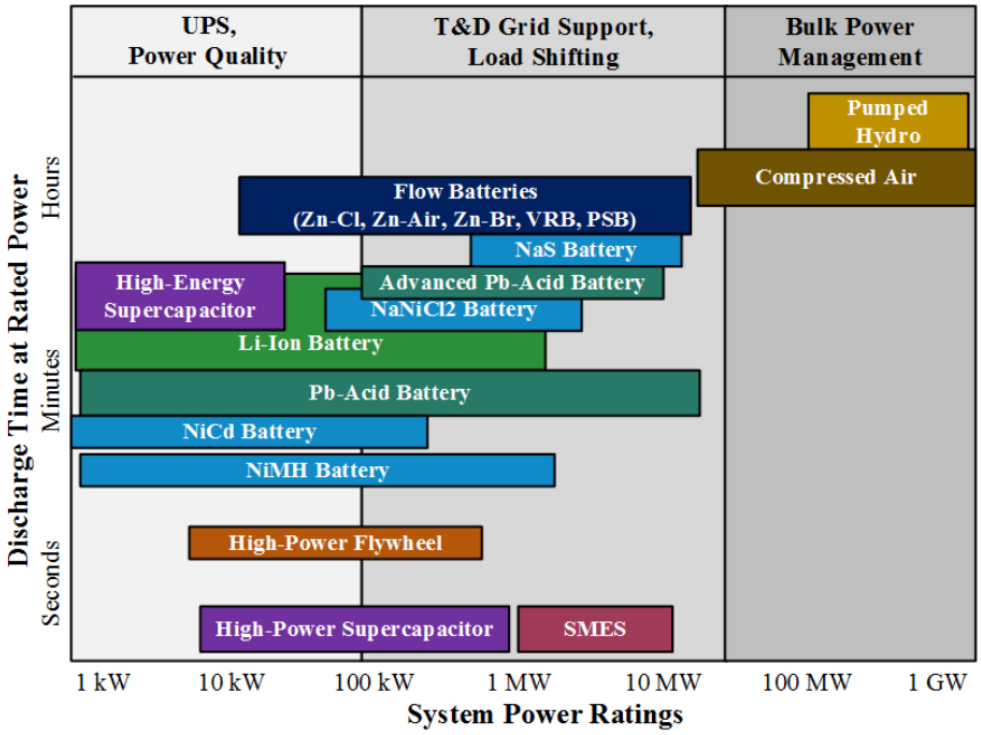

Figure 1.1 *Conseptual discharge times and power ratings of various energy storages. [5]*

Lithium-ion batteries must have precise monitoring of the state of charge (SoC) and the state of health (SoH) [6,7]. The battery SoC indicates how much battery capacity is available of its fully charged state. The battery SoH indicates how much a battery has aged from its beginning of life (BoL), which is usually defined by the capacity fade or the internal resistance increase of the battery [8]. Also, for the second-life use and recycling perspectives, the SoH estimation becomes even more important. The battery SoC and SoH are difficult to monitor accurately due to the complex and unpredictable chemical reactions inside the battery and degradation mechanisms which are not completely understood yet [9]. Moreover, battery quantities such as voltage, temperature, charge/discharge current and internal resistance have a non-linear dependency on the SoC and the SoH [4, 6]. However, battery internal impedance is highly dependent on the SoC and SoH and in literature [4, 6, 10, 11], these quantities have been successfully estimated with battery internal impedance measurements. In [4] the battery aging on cycling was studied using impedance measurements and in [10] battery aging during storage aging was studied using the same method. In [6, 11] battery internal impedance dependency on the SoC was studied.

Impedance measurements of a battery are usually carried out with electrochemical impedance spectroscopy (EIS), where sine waves of different frequencies are perturbed to the system. This is a matured and robust method for impedance measurement, but it requires a lot of computational effort and is also very slow method. Fortunately, many other methods have been studied. In [11], a pseudo-random binary sequence (PRBS) was used to execute impedance measurements and in [6] a ternary sequence was used. These methods are based on broadband excitations so they cover the necessary frequency areas only by one injection. Estimation of the battery aging using impedance measurements is still very slow because the battery should be aged for a few years in a controlled environment to get reliable data of the aging. Also, battery charging and discharging to the desired state of charge is time-consuming.

Precise modeling of the battery and emulation of the battery operation with different quantities increase the testing and developing efficiency [12]. Battery emulation has been researched in many publications [12–20]. However, battery impedance emulation have not been studied much and aging emulation have not been studied at all. In [19, 20], the battery internal impedance was emulated and modeled using an accurate local model network and model predictive control.

In this thesis, Li-ion battery internal impedance and aging are modeled and emulated. Emulation is a process which tries to imitate the operation of a chosen device, in this case Li-ion battery, with an external hardware. With a battery emulation, the battery SoC and SoH can be changed instantly without time-consuming aging tests and charging/discharging. An equivalent electrical circuit (EEC) is chosen for modeling these quantities. The EEC consists of different electrical components which model different areas in the battery impedance spectra. The battery is emulated using a Power Hardware-in-the-Loop (PHIL) simulation with a controlled DC voltage source. The model of the battery for the PHIL simulation is implemented in the dSPACE real-time simulation platform.

The aim of this thesis is to construct the battery aging emulation setup which can be used further for researching a battery aging from the battery internal impedance. The setup can also be used for studying different renewable energy sources which needs battery dynamics alongside a photovoltaic system, for example. This is also useful for a battery development process when a prototype of a battery can be tested. Furthermore, this setup provides explicit repeatability of the tests.

The thesis is divided into the following sections. The second chapter describes the basic theory of electrical energy storages. In the third section, the modeling and chemistries of lithium-ion batteries are covered and also the basic concept of aging. This section also shows the simulations of the modeled impedance and the impedance measurement techniques and excitation signals are described in section four. The fifth section represents the measurement and emulation setup and shows the results.

2. ELECTRICAL ENERGY STORAGES

A battery is an electrochemical device used for storing electricity. Batteries can be divided into two main groups: primary batteries and secondary batteries. Primary batteries are disposable and thus, can only be used to deliver a single discharge. Secondary batteries, on the other hand, are capable of multiple discharge-charge cycles. In this thesis, only secondary batteries are considered. The battery consists of either in series or series-parallel connected, electrolytic cells (EC), which can either generate electricity from chemical reactions or use electricity to generate chemical reactions. The main components of an electrolytic cell are positive and negative electrode, electrolyte, separator, and casing. [21] A solid electrolyte interface (SEI) may also be considered as one of the components of an electrolytic cell in lithium-ion technologies [22]. This will be discussed later in this thesis. A principal scheme of an electrolytic cell, in this case, a galvanic cell, is shown in Figure 2.1. The electrodes are separated with an electrolyte, which can conduct ions between the electrodes but is not electrically conductive. Conductive electrolyte would cause an internal short-circuit and/or self-discharge. Electrodes should be as close as possible to each other to minimize the internal resistance, but not touching. Thus, electrodes are insulated with a separator, which is a porous and thin insulating material. [21]

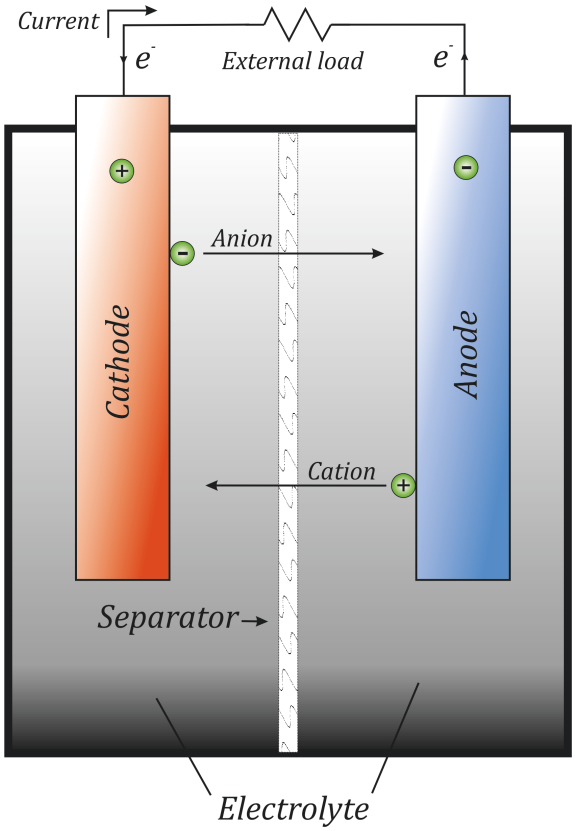

Figure 2.1 *Schematics of an electrolytic cell during discharge. Adopted from [21]*

The electricity generating chemical reactions occur at the two electrodes, which are made of chemicals known as the active material. The active material is attached to a metal component known as a current-collector. The active material undergoes reactions which can be presented as

$$M \Longleftrightarrow M^{x+} + xe^{-} \tag{2.1}$$

for negative electrode and

$$xX + xe^{-} \Longleftrightarrow xX^{-} \tag{2.2}$$

for positive electrode, where M is a metal, X is an reducing agent and x is a number of electrons. The arrows refer to the direction of the reaction: from left to right discharge and from right to left charge. When a battery is discharging, the negative

ions move towards the negative electrode and positive ions move to the positive electrode. Reaction at the negative electrode is called oxidation reaction and at positive electrode a reduction reaction, which are also known as an anodic and a cathodic reaction, respectively or simply redox reaction. In (2.1), the metal is the oxidizing agent so it loses an electron and is reduced while in (2.2) the reducing agent gains an electrode and is oxidized. In the redox reaction, the reduction and oxidation reactions occur always simultaneously and cannot occur separately. When charging, the flow of the ions is reversed. [2, 21]

2.1 State of charge

The state of charge (SoC) of a battery indicates the available charge that can be drawn from the battery [21]. The SoC affects significantly to the properties and dynamical behavior of the battery, and it can be defined as a ratio between the available capacity and nominal capacity of the battery

$$SoC = \frac{Q_a}{Q}, \tag{2.3}$$

where Q is a nominal capacity of the battery and Q_a is the available charge [15].

One of the conventional methods of the SoC estimation is Coloumb counting or ampere-hour counting [2]. The method is easy to implement and has a low need for computational power, thus, it is widely used in the estimation of the battery SoC. In its simplicity, the method is based on integrating the charging or discharging current and dividing it by battery capacity

$$SoC(t) = SoC_{init} - \frac{1}{Q}\int_0^t i(\tau)d\tau \tag{2.4}$$

where SoC_{init} is $SoC(t)$ at $t = 0$. Instead of the SoC, the depth-of-discharge (DoD) is sometimes used which is a complement of the SoC [8]. Although the Coloumb counting is an easy method for the SoC estimation, it has several limitations. The method requires a precise starting point to accurately estimate the SoC. Coloumb counting also depends considerably on the current measurement and its accuracy. A slight 1% current measurement error of the maximum discharge rate could accumulate in much larger error if the battery is charged in a longer period of time

or in smaller charge rate [2]. The usefulness of Coloumb counting decreases as the battery State of health decreases [8].

The SoC has a high impact on battery open-circuit voltage. The discharge curve, where the battery open-circuit voltage dependency on the SoC, is presented in Fig. 2.2

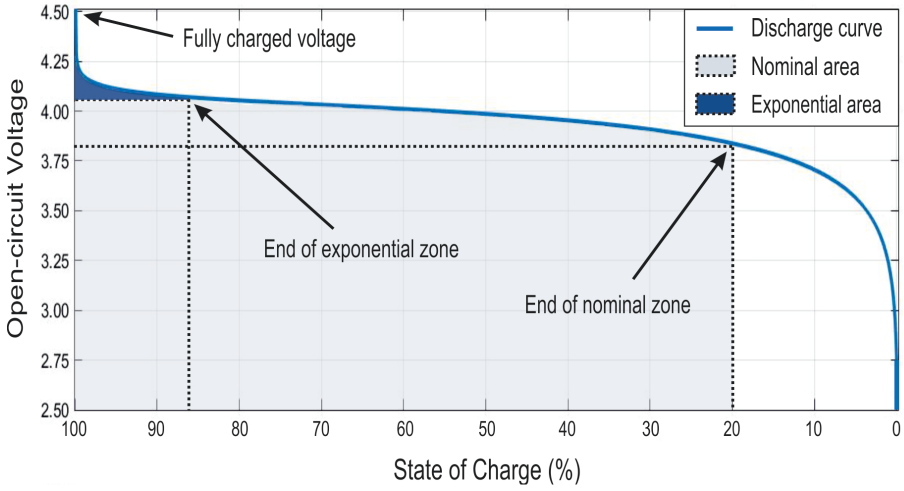

Figure 2.2 *Simulated Li-ion battery open-circuit voltage dependency on the SoC. Adopted from [23]*

The discharge curve in Fig. 2.2 is calculated using a combination of following models [24]:

- Shepherd model:

$$y(k) = E_0 - Ri(k) - \frac{K_1}{SoC(k)} \tag{2.5}$$

- Unnewehr universal model:

$$y(k) = E_0 - Ri_k - K_2 SoC(k) \tag{2.6}$$

- Nernst model:

$$y(k) = E_0 - Ri_k + K_3 \ln(SoC(k)) + K_4 \ln(|1 - SoC(k)|) \tag{2.7}$$

In these models, $y(k)$ denotes the cell terminal voltage in discrete time, E_0 is the constant voltage source, R is the internal resistance and $K_{1...4}$ are constants to fit the model to the data [8]. The combination of these models is more accurate than any of these models alone and it is described as

$$OCV(k) = E_0 - K_2 SoC(k) + \frac{K_1}{SoC(k)} + K_3 \ln(SoC(k)) + K_4 \ln(|1 - SoC(k)|) \tag{2.8}$$

The combined model is used later in this thesis to model the open-circuit voltage dependency on the SoC.

2.2 State of health

The battery state of health (SoH) indicates how far the battery is progressed from its beginning of life (BoL) toward the end of life (EoL). The battery end of life depends on the application and may have several definitions. Commonly, it can be stated that when the battery can no longer provide the minimum power, energy and standby time for the needs of the application, the battery is at the end of its life and needs replacement. A common definition for the SoH is a ratio between nominal capacity and initial nominal capacity. At BoL the value is 1 and 0 at EoL. According to [25], the SoH may also be defined by the ratio between the remaining charging times and the maximum charging times. Three main observable effects caused by internal processes in battery lead to the reduction of the battery SoH: capacity fade, impedance growth, and increased self-discharge. [2]

When the available energy and charge capacity of the battery decreases over time, it is called capacity fade. Capacity fade occurs when lithium ions or electrons cannot reach to the active material. In addition, it can also be caused by several other reasons, as for example, damaged electrode in macroscopic or microscopic level. Furthermore, active materials may lose the connection to the current collectors. 80% of the initial capacity is usually considered as a criterion for EoL. [2]

The battery impedance growth is caused by mostly the same reasons than capacity

fade but in case of lithium-ion batteries, which use carbon as an anode material, a solid electrolyte interface (SEI) growth leads to increase in impedance. The formation of SEI will be discussed later in this thesis in the section 3.3. In addition, loss of active materials lead to reduced reaction surface area which also increases the impedance. Furthermore, the degradation of the electrolyte has a contribution to the impedance growth. [2]

The self-discharge means that the battery will gradually discharge and lose the charge although it is not connected to any load. Self-discharge is caused by electrochemical reactions inside the cell. The measure of how quickly a cell will lose its capacity is called self-discharge rate. The rate is dependent on the battery chemistry and storage temperature. Li-ion batteries, for example, have relatively low self-discharge rate compared to other chemistries. Furthermore, storing the battery in higher temperatures increase the self-discharge rate. Battery self-discharge rate increases during battery aging. Since the self-discharge rate increase during aging, the available standby time of the battery is reduced. [2]

2.3 Energy density

Energy density of a battery is mostly determined by battery chemistry and the design of the cell, and it can be expressed as energy with respect to mass (Wh/kg) or energy in respect to volume (Wh/l). When designing a battery for EV or other mobile applications, energy density per volume is an important characteristic. The battery may be optimized to be an energy battery or a power battery. Energy-dense-batteries maximize the energy content and power-dense-batteries maximize to power content of the stored energy. When optimizing the battery to be an energy-dense, its power content is reduced and vice-versa. Energy batteries are used in cell phones and computers while power batteries are used in cars as a starter battery. [21, 26]

2.4 Cycle-life

The age of the battery can be described by its cycle-life which is a number of charge-discharge cycles that can be obtained until the capacity of the battery has dropped to 80% of the initial capacity. The definition may differ for the application where the battery is used but the 80% can be used as a rule of thumb. One cycle is defined when the depth of discharge is 80% or when when the state of charge is dropped to

20% of the nominal value. When the cycle-life is evaluated it is important to know the C-rate of the charge and discharge. C-rate is the rate of charge or discharge in amperes and is is declared relative to the rated capacity of the battery. Furthermore, higher DoD shortens the cycle-life. [2]

2.5 Storage life

A battery storage-life, also known as shelf-life, describes how long an unused battery can be stored before it can no longer meet the specified requirements criteria for the application. Usually the battery is at the end of its life when 80% of the initial capacity is left. For lithium-ion batteries, storage-life is somewhere between 9-12 years. [22] The temperature in which the battery is stored affects the storage life as lower temperature slows down the side reactions [26].

2.6 Calendar life

A calendar life describes that the battery will eventually lose the requirements for the application regardless of whether it is used or not. The calendar life for lithium-ion batteries can be as long as 10 years. [26]

2.7 Temperature

Battery manufacturers usually give a maximum and minimum operational temperature limits. Out of these limits batteries may still operate as designed but the performance can significantly decrease and the battery will degrade faster than in normal operating temperatures. High temperatures not only increase the regular reaction rates, but also side reaction rates known as corrosion reactions. Corrosion reactions consume the SEI layer inside the battery, which is one of the main aging factor. [22] High temperatures may also increase gas inside the battery and cause internal pressure increase and even an explosion [27]. At lower temperatures, the reaction rates decrease and ions move slowly between the active materials. However, discharge operation of a battery at low temperatures is improved compared to charging, because discharging of the battery generates heat. [22]

2.8 Internal impedance

When the battery is connected to a load, the measured voltage of a battery is always lower than its open-circuit voltage. This is caused by the internal impedance of the battery, which is realized both by the polarization losses and the ohmic losses. The polarization losses are caused by non-linear reactions in the battery electrolyte and electrodes while the ohmic losses are perceived as resistive losses determined by Ohm's law. The battery SoC and discharge/charge current affect mainly on the polarization losses while the ohmic losses are dependent on the battery SoH. Thus, the battery impedance measurements provides valuable information about the battery SoC and SoH. The polarization losses and the ohmic losses are discussed in more detail later in this thesis. [11, 21, 28]

3. LITHIUM-ION BATTERIES

Lithium-ion batteries were commercialized in early 90's [29, 30]. Lithium-ion batteries operate according to so called "rocking-chair" method. In lithium-ion cell, both electrodes are made of materials which can absorb lithium ions (Li^+) without disturbing or changing the material itself and the ions wont make a covalent bond between the active material. This phenomena is called intercalation. When the battery is discharging, the anode releases these intercalated ions which then move towards the cathode through the electrolyte and separator. Again, the ions are then intercalated to the cathode material. [31,32] A schematic of lithium-ion cell is shown in Fig. 3.1

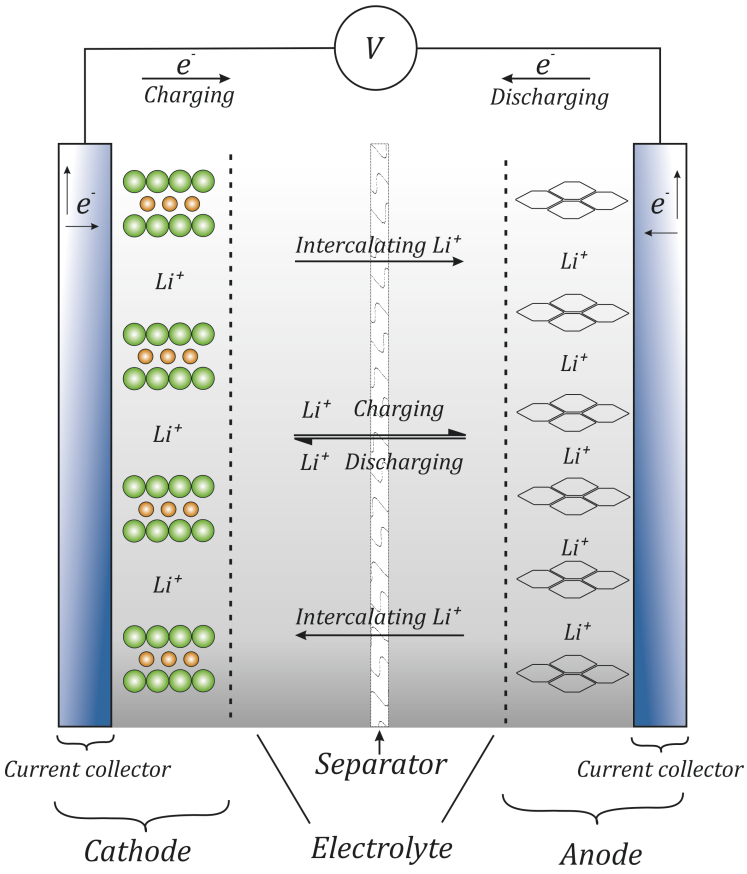

Figure 3.1 *Schematic representation of a lithium-ion cell*

Reaction equations for lithium-ion battery chemistry with lithium metal oxide as cathode and graphite anode can be presented as

$$LiMO_2 \Longleftrightarrow Li_{1-x}MO_2 + xLi^+ + xe^- \tag{3.1}$$

for positive electrode and

$$C + xLi^+xe^- \Longleftrightarrow Li_xC \tag{3.2}$$

for negative electrode. The whole reaction can be written as

$$LiMO_2 + C \Longleftrightarrow Li_{1-x}MO_2 + Li_xC \tag{3.3}$$

The same process realizes in these equations as in (2.1) and (2.2). The oxidizing agent of this reaction is the metal $LiMO_2$ so it loses an electron and is reduced while the reduction agent is the C, which gains an electron and is oxidized. [33]

3.1 Lithium-ion battery chemistries

Early lithium based batteries used metallic lithium as anode material and lithium-metal insertion oxide as cathode material. Although this technology gave exceptional energy density it suffered from safety and reliability issues compared to other commercial secondary batteries. The intercalation phenomena regarding the use of graphite anode was the key for the commercialization of Li-ion batteries. It gave the guarantee of safety and reliability, and greatly increased the lifetime of Li-ion battery. Therefore, the graphite anode is still the dominating material in the Li-ion battery markets. [29]

Battery chemistry is used to specify the materials used in electrodes. For lithium-ion batteries, the battery chemistry refers to the material of positive electrode because negative electrode material is usually carbon, in the form of graphite or an other amorphous material. The most common lithium-ion battery cathode materials are listed in Table 3.1

Table 3.1 *Common Li-ion battery chemistries [33]*

Battery chemistry	Cathode material	Energy density	Cell voltage
Lithium cobalt oxide	$LiCoO_2$	140 Wh/kg	3.7-3.9 V
Lithium nickel-manganese-cobalt oxide	$LiNiMnCoO_2$	170 Wh/kg	3.8-4.0 V
Lithium manganese oxide	$LiMn_2O_4$	120 Wh/kg	4.0 V
Lithium iron phosphate	$LiFePO_4$	100 Wh/kg	2.3-2.5 V

3.2 Lithium-ion battery modeling

Modeling the cell or a battery pack is important for simulating dynamical operation of the used battery system. Knowing the dynamical performance of the battery is important so that right battery for the right purpose can be chosen. Battery models can be divided into four different categories from the least accurate to the most

accurate: ideal model, black box model, equivalent electrical circuit (EEC) model and physical model. The ideal model is the most simple and usually not accurate enough for most applications. The ideal model is also known as linear model as described in the next section. The physical model consists of differential equations and thus, it is the most accurate, but also too complex in terms of computational effort. The EEC is gray box model, which reproduces the dynamical behavior of Li-ion battery based on electrical elements representing different physicochemical properties inside the battery [34].

3.2.1 Linear model

The most straightforward electrical model of the LIB is the internal resistance model, also known as a linear model, which can be seen in Fig. 3.2. It consists of voltage source and a resistor, which represent the open circuit voltage (OCV) and the internal resistance of the cell, respectively. [7]

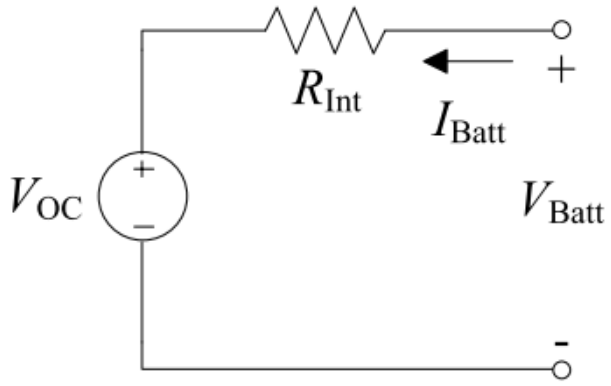

Figure 3.2 *Internal resistance electrical model of LIB [7]*

Electrical equivalent circuit equation for the internal resistance model can be written as

$$V_{Batt} = V_{OC} + R_{int} \cdot I_{Batt} \tag{3.4}$$

Only the current flowing through the resistance causes a voltage drop to the terminal voltage V_{batt} and thus, this model is not accurate enough to simulate the transient

behavior of the battery [11]. Moreover, the voltage source and resistor have fixed values and they are not dependent on the SoC, SoH and temperature.. Furthermore, it does not contain any parallel connected capacitor and resistor branches, which are able simulate charge transfer and double-layer dynamics, which are important processes in batteries. Thus, more accurate models are needed and they are described in next sections. [7, 35]

3.2.2 Shepherd model

Shepherd model is a well-known voltage-current model developed in the 1960s for constant current discharge described as

$$v = E_0 - Ri - K\frac{Q}{Q - it}i + Ae^{-B\frac{it}{Q}}, \tag{3.5}$$

where E_0 is an open-circuit voltage of the battery, K is a polarization resistance coefficient, Q is a capacity, A is the exponential zone amplitude, B is the exponential zone time constant inverse and it is the current computed as

$$it = \int_0^t i(\tau)d\tau. \tag{3.6}$$

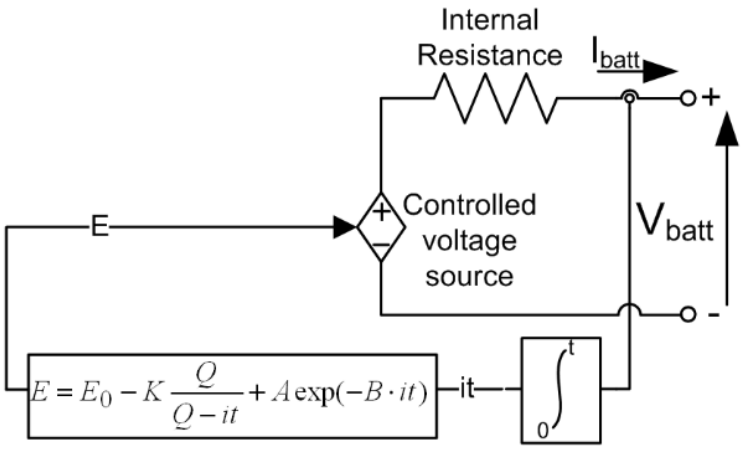

Figure 3.3 *Controlled voltage source model [23]*

substituting Eq. (3.6) to Eq. (3.5) gives

$$v = E_0 - Ri - K\frac{1}{SoC}i + Ae^{-B(1-SoC)} \tag{3.7}$$

The model has the same basic elements as linear model introduced above but including a controlled voltage source as seen in Fig. 3.3. The Shepherd model accurately models the battery terminal voltage as a function of SoC assuming that the model parameters are determined correctly. Usually the parameters for this model can be extracted from the manufacturer's curve by fitting. However, since the battery is nonlinear system this model is based on a few assumptions. The internal resistance is assumed to be constant and does not depend on the current, the parameters are assumed to be same during charging, the capacity of the battery is not dependent on the current (i.e. no Peukert effect), the affection of temperature is neglected and the effect of self-discharge is neglected. [23] This model can also be used for battery open-circuit voltage dependency on the SoC like discussed in section 2.1.

3.2.3 Randle's model

A typical Randle's model consists of a parallel RC circuit in series with the internal resistance of the battery. Depending on the desired accuracy of the model, more RC circuits can be added to the model. This so called n-order Randles model is presented in Fig. 3.4.

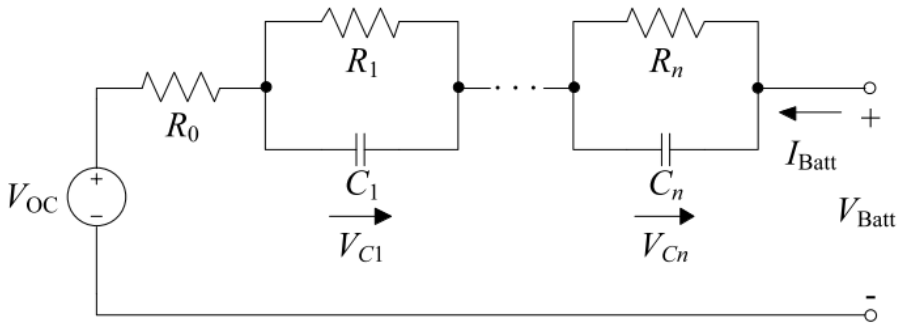

Figure 3.4 *n^{th} order Randles model [7]*

With the added capacitors, the model is now able to simulate the transient behavior of the battery [7]. The main advantage of using several RC circuits is that one of

the circuits can model the low frequency responses and the other one high frequency responses in the case of second order model. Second or third order models are used most of the times because of their good relation between accuracy and complexity [7]. State space representation for the nth order Randles model can be written as

$$\begin{bmatrix} \dot{V}_{C1} \\ \vdots \\ \dot{V}_{Cn} \end{bmatrix} = \begin{bmatrix} -\frac{1}{R_1 \cdot C_1} & 0 & 0 \\ 0 & \ddots & 0 \\ 0 & 0 & -\frac{1}{R_n \cdot C_n} \end{bmatrix} \begin{bmatrix} V_{C1} \\ \vdots \\ V_{Cn} \end{bmatrix} + \begin{bmatrix} \frac{1}{C_1} \\ \vdots \\ \frac{1}{C_n} \end{bmatrix} I_{Batt}, \tag{3.8}$$

$$V_{Batt} - V_{OC} = \begin{bmatrix} 1 & \cdots & 1 \end{bmatrix} \begin{bmatrix} V_{C1} \\ \vdots \\ V_{Cn} \end{bmatrix} + R_0 I_{Batt}, \tag{3.9}$$

$$v_i(s) = R_i \frac{1/(R_i C_i)}{s + 1/(R_i C_i)}, i_{batt}(s) \tag{3.10}$$

where s is the Laplace variable, R_0 is the series resistance, V_{OC} is the open-circuit voltage, R_1 and C_1 are the resistance and capacitance of the first RC branch, respectively, R_n and C_n represent the resistance and capacitance of nth RC branch, respectively. [7]

Ohmic losses

A battery always has some ohmic resistance called internal resistance. Internal resistance is formed by resistive phenomena of the current-collectors, electrolyte and electrodes. The resistance of an electrolyte depends on the electrolyte concentration, ion type, temperature, and the geometrical area where the current is flowing. The resistance of an electrolyte can be defined as

$$R_{el} = \frac{l}{\kappa A}, \tag{3.11}$$

where κ is conductivity of the electrolyte and A is the area where the current goes a length of l in the electrolyte. The unit of κ is Siemens per meter (S/m). The conductivity increases when the number of charge carriers increases in the electrolyte. The

movability of the charge carriers in the electrolyte is, however, the limiting factor of the increase in conductivity. [36]

Double-layer capacitance

When two electrodes are put in an electrolyte, the ion concentration difference between the electrodes and the electrolyte will stabilize. The positive Li-ions in the electrolyte will diffuse into electrode and thus, potential difference exist on the interface between the electrode and electrolyte. The potential difference forms an electrical field in the electrode-electrolyte interface. The interface is called electrical double-layer. The electrical double-layer acts ideally like a capacitor, but in real cells it can be modeled more accurately as a constant phase element (CPE), which is further discussed in next sections.

Charge transfer resistance

Charge transfer process of a lithium-ion battery can be described by using the Butler-Volmer equation [37, 38] as

$$I = I_0 \left[\exp\left(\frac{\alpha x F \eta}{RT}\right) - \exp\left(\frac{-(1-\alpha) x F \eta}{RT}\right) \right], \tag{3.12}$$

where I_0 is exchange current, η is over potential, F is Faraday's constant, T is Temperature, R is gas constant, α is reaction order and x is the number of electrons. The Eq. (3.12) is highly non-linear and thus, the charge transfer resistance R_{ct} is also non-linear. This is why a battery can not be considered as a linear load [39]. The charge transfer resistance R_{ct} is further discussed in next section, where it is a part of ZARC element.

Constant phase element

Constant phase element (CPE) models the constant phase behavior of the cell at low frequency range. It is also used to improve the accuracy of model so that RC branches are able to model the high frequency behavior in a better manner. [7]

Impedance of the CPE element can be written as

$$Z_{CPE}(j\omega) = \frac{1}{(j\omega)^d Q} \tag{3.13}$$

where Q is a generalized capacitance and d is depression factor. With depression factor equal to 1, -1 and 0, the CPE model is similar to capacitor, inductor and resistance, respectively. Usually, value from 0 to 1 is used for the d, which represents part of capacitance and part of resistance. Using the CPE element to model the impedance, the frequency response accuracy of the model is improved significantly. However, it also increases the complexity regarding the implementation of the model such that it is not as appealing as the models described earlier. The parallel connection of the CPE and charge transfer resistance is called ZARC element. Thus, impedance of ZARC element leads to equation (3.14) [40]

$$Z_{ZARC} = \frac{R_{ct}}{1 + (j\omega)^d R_{ct} C_{dl}}, \tag{3.14}$$

where R_{ct} is charge transfer resistance and C_{dl} is double-layer capacitance. [36] Impedance of the ZARC element with different depression factor values is shown in Fig. 3.5.

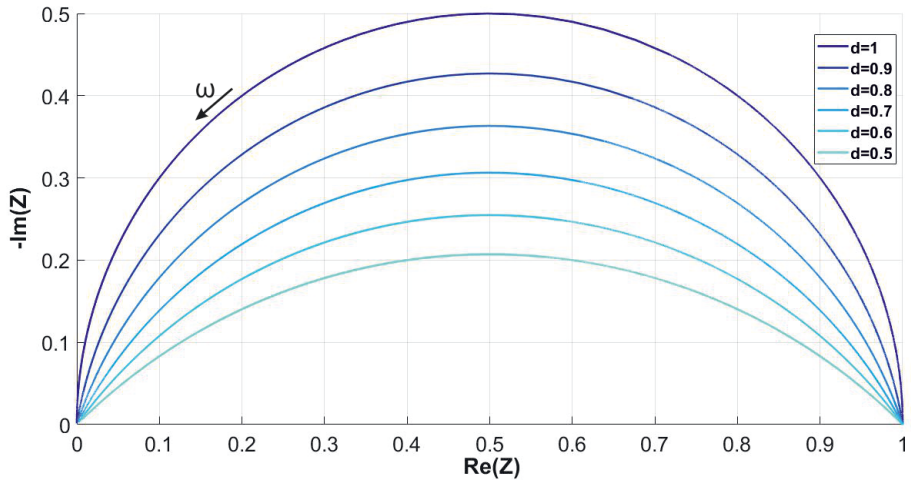

Figure 3.5 *Impact of depression factor on the ZARC element impedance*

As seen in Fig. 3.5, with depression factor equal to 1, the impedance of ZARC ele-

ment equals to the impedance of parallel RC-circuit. When decresing the depression factor, the complex plane impedance is pressed

Approximation of ZARC element

The basic impedance elements like inductance and capacitance can be directly implement in Matlab/Simulink simulation software. However, the ZARC element and Warburg impedance are more difficult to model and they need a mathematical approximations [**?**]. According to [41], the ZARC element can be approximated by using several non-linear RC circuits shown in Fig. 3.6. Increasing the number RC circuits makes the approximation of ZARC elements more and more precise at the expense of computing effort. A one proposed approximation in [41] was to model the depressed semi-circle in complex plane by using a 5 RC circuits (A...E) with different parameters. The first RC branch models the impedance of the middle section of the semi-circle and two other RC branches were placed symmetrically so that their impedance models both sides of the impedance of the first branch. These approximated semi-circles are presented in Fig. 3.7.

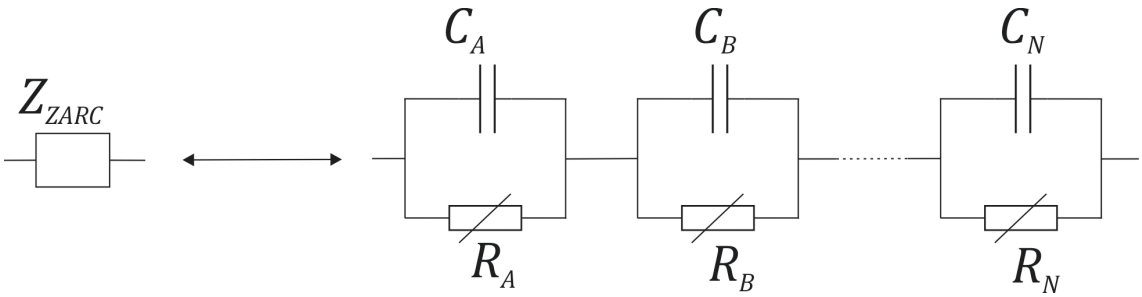

Figure 3.6 *ZARC element approximation with RC circuits. Adopted from [37]*

Impedance of the approximated ZARC element with 5 RC-circuits and the ideal ZARC element impedances with different depression factors are shown in Fig. 3.7.

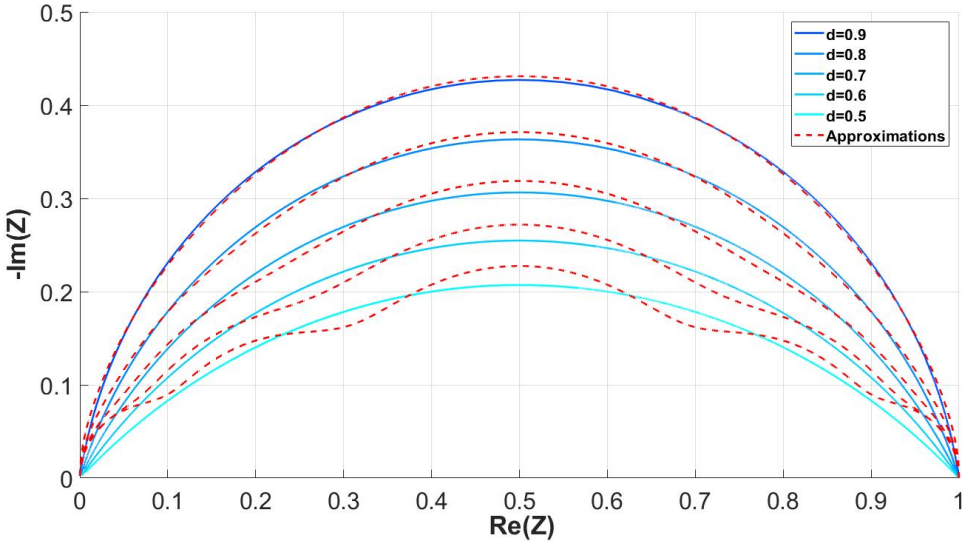

Figure 3.7 *Calculated ZARC element approximation using 5 RC-circuits with various depression factors*

As seen in the Fig. 3.7, the approximation is quite accurate when $d > 0.7$. In [41], the resistance of middle semi-circle (expressed as C) can be calculated as

$$R_C = f_1(d) \cdot R \cdot \frac{\sin(\frac{\pi}{2}d)}{1 + \cos(\frac{\pi}{2}d)}, \tag{3.15}$$

and the capacitance

$$C_C = \frac{1}{\omega_{0_{ZARC}} R_C} \tag{3.16}$$

where $f_1(d)$ is factor depending on depression factor d, R is the resistance of the ZARC element and $\omega_{0_{ZARC}}$ is the characteristic frequency calculated as

$$\omega_{0_{ZARC}} = \left(\frac{1}{RQ}\right)^{1/d} \tag{3.17}$$

The resistances and capacitances of the other four semi-circle can be calculated based on symmetry [41]. The resistances next to each side of the middle semi-circle are expressed as R_B and R_D, and they are described as

$$R_B = R_D = f_2(d) \cdot \frac{R - R_C}{2}. \tag{3.18}$$

While the capacitances of these semi-circles are calculated as

$$C_B = \frac{1}{f_3(d)\omega_{0_{ZARC}} R_B} \tag{3.19}$$

and

$$C_D = \frac{1}{\frac{1}{f_3(d)}\omega_{0_{ZARC}} R_B}. \tag{3.20}$$

The last two remaining resistances R_A and R_E, and capacitances C_A and C_E for the far right and left of the semi-circles can be calculated as

$$R_A = R_E = \frac{R - R_C - R_B - R_D}{2}, \tag{3.21}$$

$$C_A = \frac{1}{\left(f_3(d)\right)^2 \omega_{0_{ZARC}} R_A} \tag{3.22}$$

and

$$C_E = \frac{1}{\frac{1}{(f_3 d)^2}\omega_{0_{ZARC}} R_E}. \tag{3.23}$$

The factors in the equations 3.15 to 3.23 first presented in [41] are listed in the table 3.2

Table 3.2 *Factors f_1, f_2 and f_3 for the five RC-circuit approximation [41]*

d	0.5	0.6	0.7	0.8	0.9
$f_1(d)$	0.906	0.896	0.837	0.833	0.876
$f_2(d)$	0.670	0.733	0.772	0.804	0.835
$f_3(d)$	10.886	8.331	6.176	4.675	3.634

These factors are used in the emulations as a look-up table in Simulink to select the correct factro for every depression factor value

Warburg impedance

Warbug impedance models the diffusion behavior of the cell and describes the lower frequencies in the impedance spectrum. There are three different types of Warburg impedances: Semi-infinite diffusion, limited diffusion and ideal reservoir at the boundary, and limited diffusion and non-permeable wall at the boundary [38].

Warburg impedance can be defined by

$$Z_W = \sqrt{\frac{R_D}{j\omega C_D}} \cdot DL, \tag{3.24}$$

where R_D is diffusion resistance and C_D is diffusion capacitance. DL states to diffusion layer, which describes the type of the Warburg impedance, which is related to thickness of the diffusion layer. DL is equal to 1, when the layer is infinite. This type of Warburg impedance is the case of semi-infinite diffusion and it can be defined by

$$Z_W = \frac{W}{\sqrt{\omega}}(1 - j), \tag{3.25}$$

where W is a Warburg coefficient. [38] When considering the lithium-ion batteries, the diffusion process is limited and the factor DL can be defined by

$$DL = \coth(\sqrt{(j\omega)^d R_D * C_D}) \tag{3.26}$$

DL factor for Warburg impedance with limited diffusion and ideal reservoir at the boundary can be defined

$$DL = \tanh(\sqrt{(j\omega)^d R_D * C_D}) \tag{3.27}$$

and is presented as green in 3.8. [38]

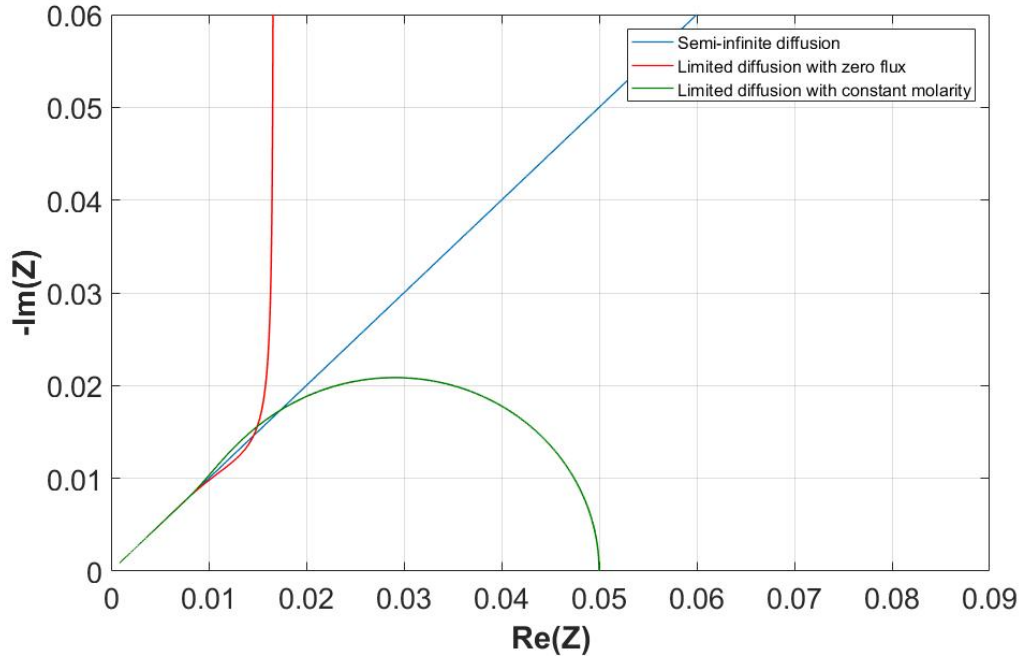

Figure 3.8 *Different types of Warburg impedances with depression factor equal 1*

Approximation of Warburg impedance

In addition to ZARC elements, the Warburg impedance cannot be implemented to the Matlab/Simulink as such, and thus, it needs an approximation [41]. The Warburg impedance can be approximated using parallel RC circuit and series capacitance. Circuit representation of this approximation is presented in Fig. 3.9.

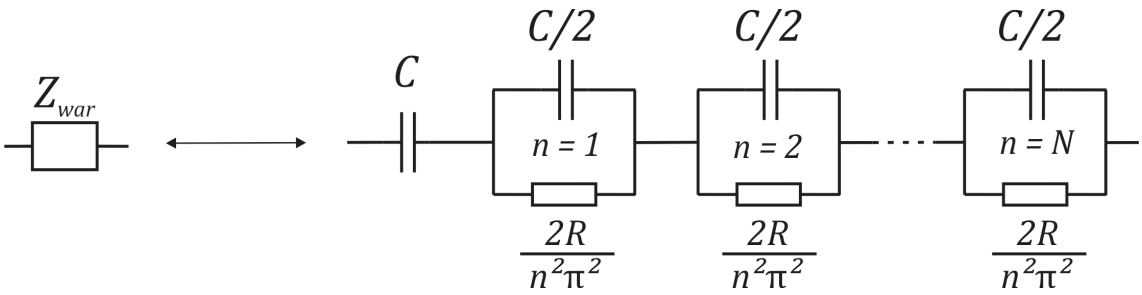

Figure 3.9 *Approximation of Warburg impedance with non-linear RC-circuits. Adopted from [41]*

Impedance of this approximation for the nth RC-circuit is

$$Z_{RC_n} = \frac{\frac{2R}{n^2\pi^2}}{1 + j\omega\frac{C}{2}\frac{2R}{n^2\pi^2}} = \frac{2R}{n^2\pi^2 + j\omega RC} \tag{3.28}$$

And for $n = N$, the approximation can be described as

$$Z_W = \frac{1}{j\omega C} + \sum_{n=1}^{N} \frac{2R}{n^2\pi^2 + j\omega RC}. \tag{3.29}$$

In [41], this approximation was used in simulations with 50 RC branches.

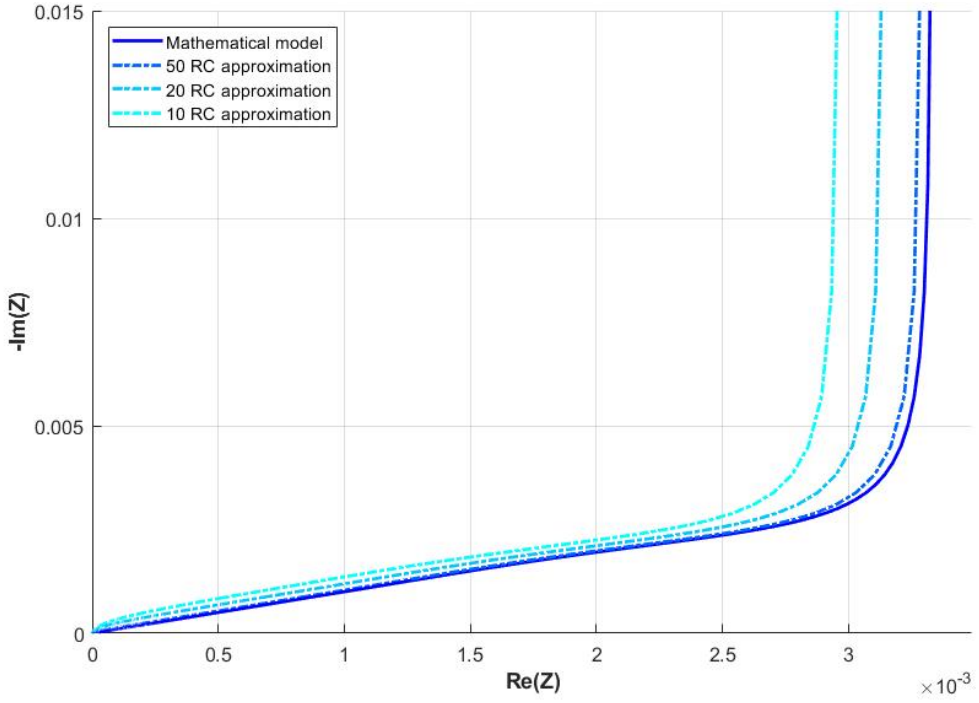

Figure 3.10 *Calculated approximations for Warburg impedance with various number of RC branches*

Combining the elements

The following modified Randle's circuit is established when combining the inductance, ohmic losses, CPE and Warburg impedance to the model. The model is used

in the impedance simulations and emulations later in this thesis.

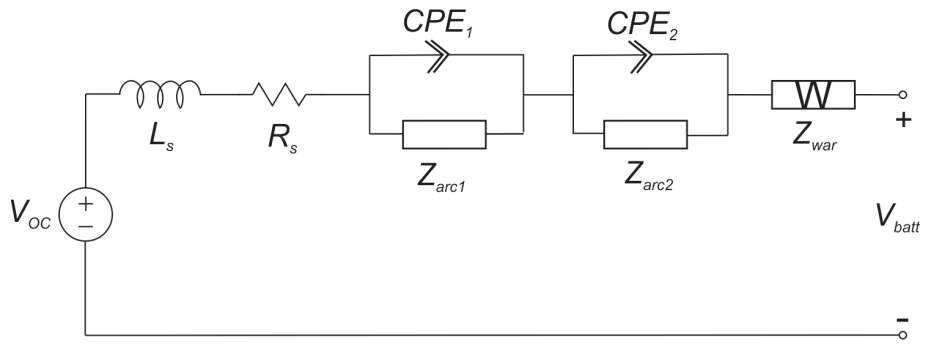

Figure 3.11 *Electrical equivalent circuit*

The total impedance of the model represented in 3.11 can be described as

$$Z_{tot} = R_s + j\omega L + Z_{ZARC} + Z_{War}, \tag{3.30}$$

where L is inductance, Z_{ZARC} is Eq. 3.14 and Z_W is Eq. 3.24 with Eq. 3.26

3.3 Lithium-ion battery aging

Lithium-ion battery aging process is complicated because of the complex electrochemical and mechanical processes that are taking place inside the battery [42]. Aging at anode and cathode has a major difference and the processes are highly determined by the operating conditions. The main aging mechanism is a growth of SEI at the negative electrode made of graphite material [43]. Also, decomposition of electrolyte leads to an increase in the internal resistance due to overcharging and over-discharging of the battery [9]. Since the Li-ion battery cathode materials differs a lot, their aging properties should be discussed by case to case depending on the material, this section focuses mostly on the aging of anode.

3.3.1 Solid electrolyte interface (SEI) formation

Most of the commercial lithium-ion batteries has a graphite, carbon, titanate or silicon as anode material [44], and thus, most of the research done considering aging

of anode. SEI is now a universally known concept originally proposed in [45]. The layer acts like interface between metal and solution and has properties of solid electrolyte. Lithium ions can move through this layer but it prevents electrons to reach the molecules of electrolyte. Formation of the SEI and other aging mechanisms on the negative electrode are presented in Fig. 3.12

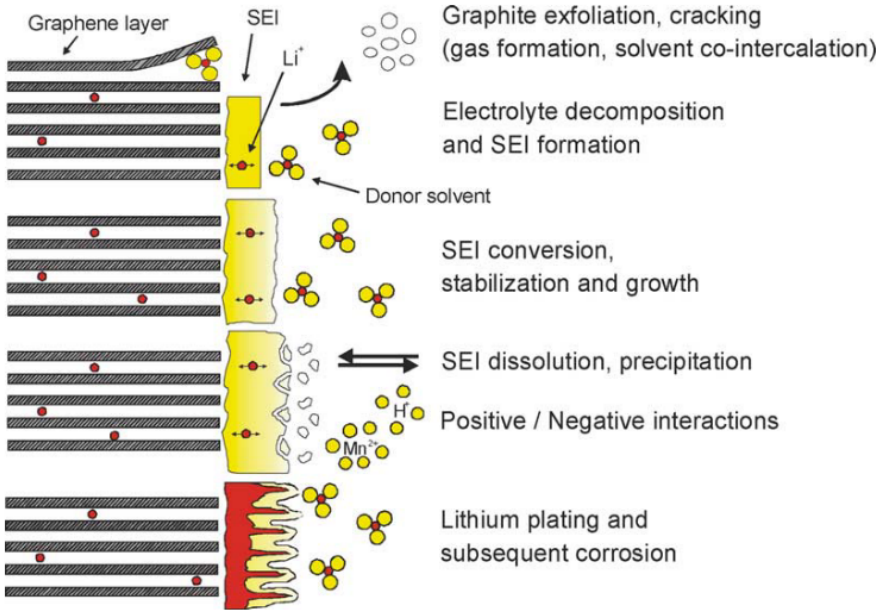

Figure 3.12 *Formation of solid electrolyte interface [9]*

The formation of SEI is due the reactions between the carbonaceous anode and the electrolyte. The creation of SEI occurs naturally during the first charge cycle of the battery when the lithium reacts with the graphite [29]. It is a natural protective layer between the electrolyte and the anode [43], and it ensures performance and the safety of the lithium-ion battery [46].

3.3.2 Lithium plating

The reversible intercalation phenomena is the main advantage of using graphite as a anode material like discussed in 3. However, in some cases the Li-ions may form a metallic lithium at the electrode surface which is not a fully reversible process and dissolution of Li may occur. Dissolution of Li-ion may for other than lithium ion compounds. While the growth of SEI layer mostly increase in higher temperatures, most of the time the lithium planting is occurring during low operational

temperatures. [29]

3.3.3 Aging of cathode

While most of the aging processes in anode are based on the graphite as anode material, the materials used as cathode may vary a lot and thus, the aging of cathode might be different for used materials. Most used cathode material in lithium-ion batteries is $LiCoO_2$. When using too high cell voltages than $4.35V$, this material may decompose and results an irreversible capacity loss and thermal runaway. With increasing cycle numbers, an increase of charge transfer resistance can be observed at this electrode material. [47]

4. BATTERY IMPEDANCE MEASUREMENT METHODS

System models can be generally divided to parametric and non-parametric models. Parametric models can be described by a finite amount of parameters and the parameters are not dependent on the data length. In non-parametric modeling, the number of parameters are not fixed and they grow with the data length. An example of non-parametric model is a frequency response function (FRF) of a system [48]. Identification of a lithium-ion battery is difficult to do with parametric methods because of its complex and non-linear dynamic behavior and complex model structure. Thus, non-parametric methods are preferred.

4.1 System identification

Considering the basic control theory, linear time-invariant (LTI) system can be identified by its impulse-response function $g(t)$. Identified system is perturbed with input $x(t)$ excitation signal producing the output response $y(t)$ as seen in Fig. 4.1 [49].

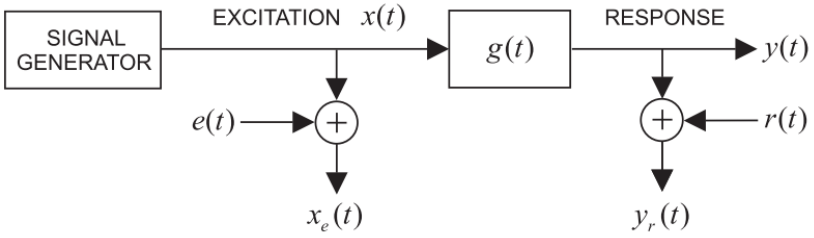

Figure 4.1 *Typical measurement set up for non-parametric modeling [49]*

In Fig. 4.1, the measured input and output signals, $x_e(t)$ and $y_r(t)$ are assumed to be corrupted by white noise denoted by $e(t)$ and $r(t)$. The signals in Fig. 4.1

are in time-domain so to extract the frequency content of the signals a Fourier-transformation is needed, which can be described as

$$G(jw) = \int_{-\infty}^{\infty} g(t)e^{-jwt}dt, \tag{4.1}$$

where $G(jw)$ is the signal in frequency domain. In real systems, a discrete Fourier transform (DFT)

$$X_k = \sum_{n=0}^{N-1} x_n \cdot e^{-\frac{i2\pi}{N}kn} \tag{4.2}$$

is usually used because continuous signals can not be handled in digital systems. [50] The system frequency response in Fig. 4.1 without the noise can be expressed as

$$G(jw) = \frac{Y(jw)}{X(jw)} \tag{4.3}$$

When measuring the impedance of a battery, Ohm's law can be used to Eq. (4.4) and expressed with current and voltage as

$$Z(jw) = \frac{U(jw)}{I(jw)}, \tag{4.4}$$

where the input of the system is now current $I(jw)$, output is voltage $U(jw)$ and transfer function is impedance $Z(jw)$.

4.2 Sine sweep

Sine sweep is a common method used in system identification. In the method, a sine wave of fixed frequency and amplitude is injected to the identified system and the voltage response is measured. The frequency is then increased to desired value for the next measurement. A generated sine wave at one frequency can be determined as

$$x(t) = A \sin(2\pi f t), \tag{4.5}$$

where A is a amplitude of the perturbation and f is frequency. The sine sweep has a high Signal-to-Noise Ratio (SNR) compared to other perturbation methods because only one frequency is injected to the system at a time. The SNR can be increased further by increasing the amplitude of the signal. The sine sweep method is also convenient for identification of non-linear systems due to fact that its harmonic content is visible [50].

The sine-sweep method typically provides a reliable frequency response of a system, but the method is not suitable for most practical applications (for example EV, HEV) because of several reasons. Firstly, the devices used to generate sine sweeps are complex and expensive, because the sine wave signal is continuous and digital systems would require a high amount of bits to estimate the signal accurately. Secondly, sine sweep perturbations with large bandwidth and resolution are particularly slow, because with each frequency generated, it is useful and even necessary to wait before the transient of each frequency step is over. [34]

4.3 Pseudo-random binary signals

Pseudo-random binary sequence (PRBS) is a deterministic broadband periodic binary signal. Thus, it has only two levels, which can be switched at certain event points. Maximum length binary sequence (MLBS) is the most used class of pseudo-random binary signals, because it is easy to generate in hardware using shift registers with XOR feedback. The MLBS is periodic with period $T = N\Delta t$, where N is an odd integer. Within one period, there are $(N + 1)/2$ intervals when the signal is at one level and $(N - 1)/2$ intervals when it is at the other level. The length of the MLBS sequence is $N = 2^n - 1$, where n is an integer > 1 and a number of stages in the shift register. For example, with five-stage shift register, shown in Fig. 4.2, the length of the sequence is $2^5 - 1 = 31$. The sequence is generated so that the feedback to the first stage is the modulo-2 sum of the last stage and one or more of the other stages. [51]

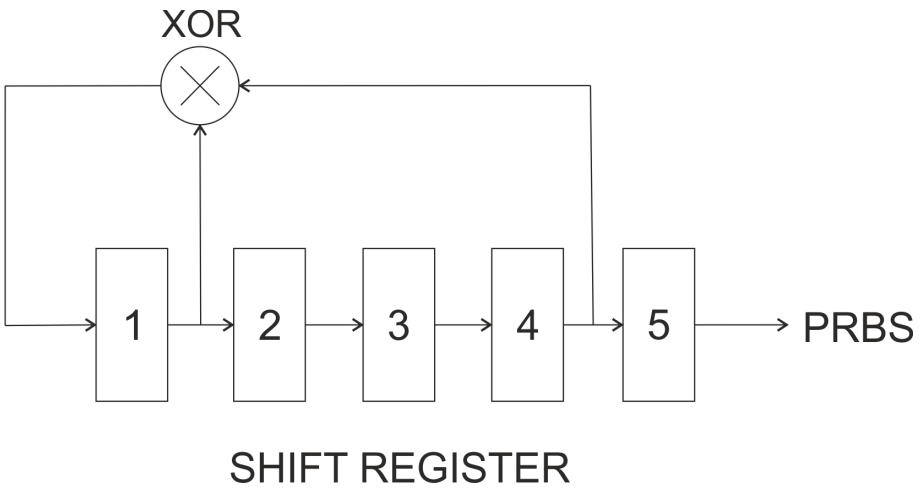

Figure 4.2 *5-bit shift register with XOR feedback*

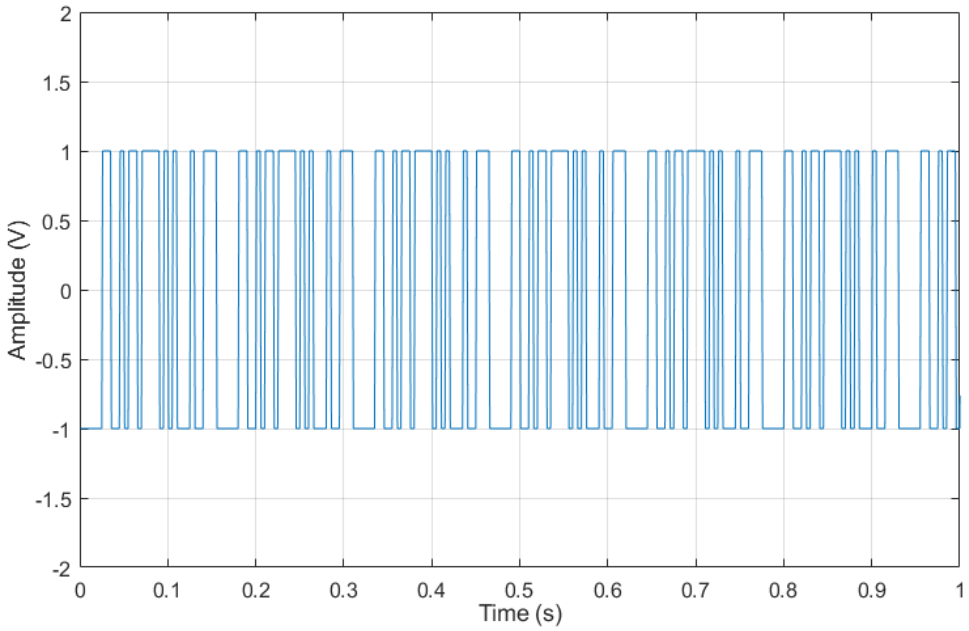

Figure 4.3 *10 periods of 5-bit PRBS with 1 kHz generation frequency*

The power spectrum of MLBS can be defined as

$$\Phi_{MLBS}(q) = \frac{a^2(N+1)}{N^2}\frac{\sin^2(\pi q/N)}{(\pi q/N)^2}, q = \pm 1, \pm 2, ... \tag{4.6}$$

where q denotes the sequence number of the spectral line, a is the amplitude of

MLBS and N is the length of the sequence. The highest power value is at the first harmonic, i.e. when $q = 1$, as seen in (4.6). The harmonics are seen as energies of the signal at certain frequencies and they occur at frequencies q/T_p, where T_p is a time length of one signal period. The power spectrum of the MLBS presented in Fig. 4.3 is obtained from equation (4.6) and presented in Fig. 4.4.

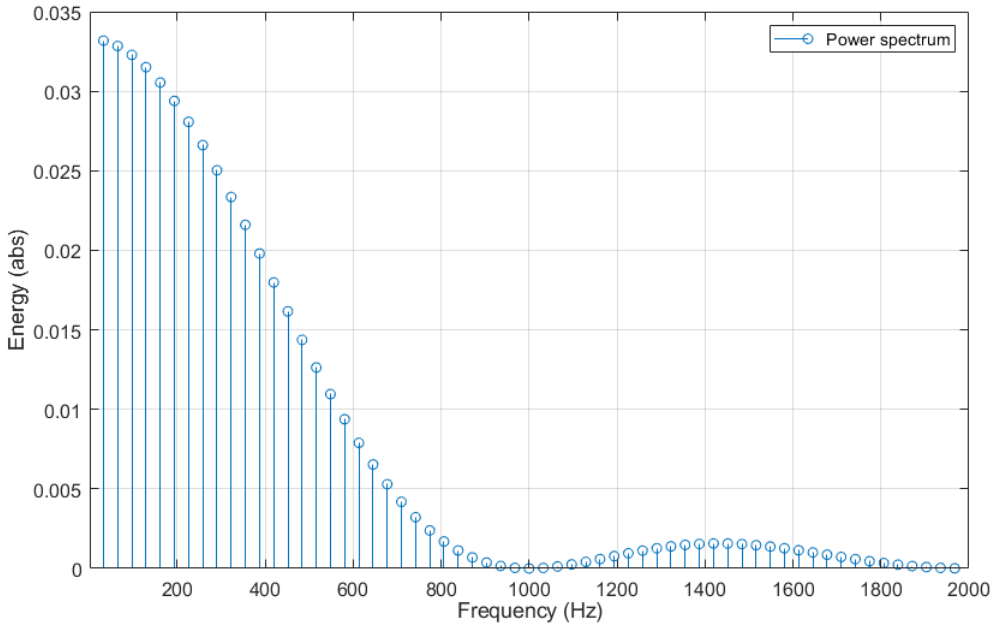

Figure 4.4 *Power spectrum of 1 kHz MLBS*

As seen in Fig. 4.4, the energy of the MLBS drops to zero at the generation frequency. The usable frequency band is only at the frequency when the amplitude of the signal has dropped to $1/\sqrt{2}$ of the first harmonic, that is, 3 dB.

The amplitude of the excitation should be selected carefully. High amplitude may cause nonlinear distortion which affects the measurements. Too low excitation may be affected by measurement noise so the signal-to-noise ratio is relatively low. The SNR can be easily increased by using several MLBS periods and averaging. The SNR increases by a factor $\sqrt{M}$, where M is a number of periods. Thus, the amplitude of the excitation can be kept low enough in order to not affect the non-linearities but still keeping the SNR high enough.

According to [6], the battery impedance measurements performed by the MLBS suffers from non-linear effects. The work in [28] presented techniques to minimize

these non-linear effects by applying ternary sequence. The ternary-sequence has a similar time- and frequency domain characteristics compared to MLBS but the signal has three levels and average close to zero. Also, the ternary-sequence can be designed in such a way that the signal even- or odd-order harmonics are suppressed. [28, 52] This increases the performance of the ternary-sequence for non-linear system, such as Li-ion battery, identification. The ternary-sequence used for a battery impedance measurements in [28] gave results that matched quite well with the classical EIS measurements.

4.4 Impedance spectroscopy

Electrochemical impedance spectroscopy (EIS) is a common technique used to characterize and model the dynamic behavior of lithium-ion batteries [53]. Typical representation of lithium-ion battery impedance spectrum [4] in complex plane is shown in Fig. 4.5, where the imaginary part of the impedance is reversed.

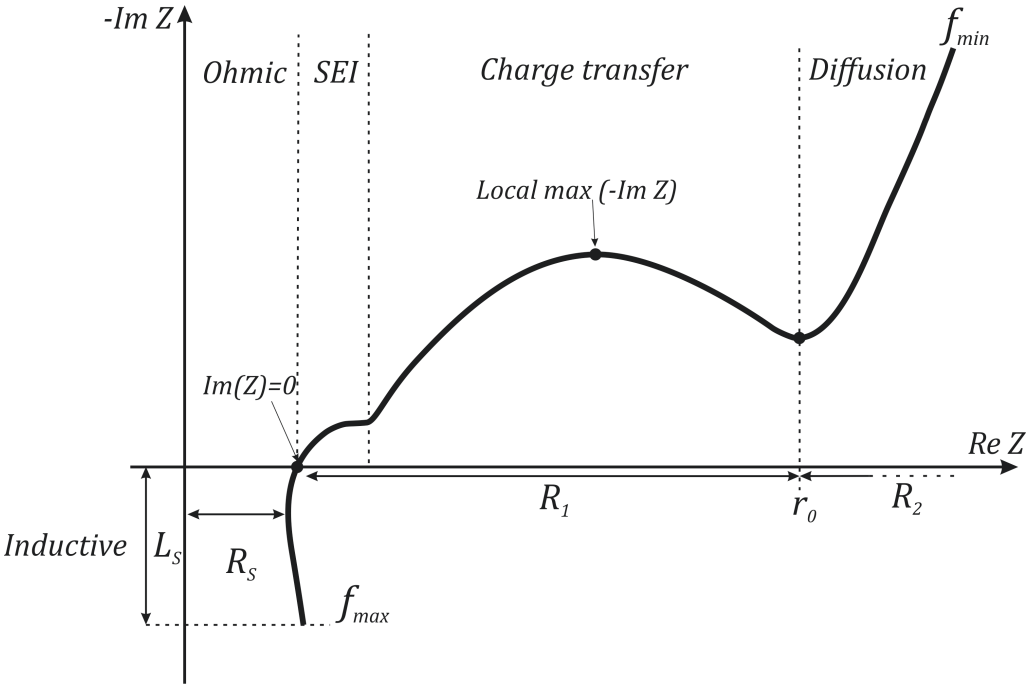

Figure 4.5 *Typical state-of-the-art battery impedance spectrum. Adopted from [4]*

Five basic characteristic points can be seen from the impedance spectrum, which describe the dynamics of the battery. The first section is below the real axis, where

the impedance spectrum shows an inductive behavior [10]. The inductive behavior is caused by conducting wires and other metallic elements of the cell. Also, a porousness of electrodes may cause inductive behavior at higher frequencies. Usually this part of the impedance spectrum is not interesting, and the measurements are done in the border of inductive and capacitive section. [53, 54]

The second section is at $Im\{Z(f)\} = 0$, where the impedance spectrum intersects the real axis. This describes the pure ohmic resistance r_o of the battery [53]. Although, the impedance spectrum crosses the real axis at certain frequency, it is actually not a pure resistance because the battery has always inductive and capacitive behavior, but at that frequency all the inductive elements are compensated by the capacitive elements of the battery. Thus, the impedance value is shown as pure ohmic resistance in the spectrum. [10, 28, 54]

The third section is the first small semicircle at higher frequencies, which is related to the SEI layer on the negative electrode or to the particle-to-particle contact of the active materials. [4, 53, 54]

The fourth section covers the larger semicircle at local maximum of the negative impedance and it correlates to charge transfer resistance combined with double layer capacitance [28]. Also, it defines the dynamic of the battery voltage response by current changes. The lower the frequency, the slower the voltage change at fast current changes. This section is usually dominating area, so it may cover the smaller semicircle caused by SEI layer. [4, 53, 54]

The fifth section is at a local minimum of the negative imaginary part, which corresponds to the direct current resistance (DCR) (r_0 on the Fig. 4.5) [53]. The DCR is a sum of the pure ohmic resistance and the polarization resistance, which is usually used to describe the power capability of the battery [53]. The lower frequencies beyond this point is caused by the diffusion process of the cell [4, 28, 54].

4.4.1 Impedance dependency on aging

Aging of the battery can be seen in the battery impedance spectrum. Therefore, the impedance spectroscopy is a widely used method to characterize the aging of batteries. [2, 4, 7, 53, 55–57]. Changes in the impedance spectra during aging on cycling can be seen in Fig. 4.6.

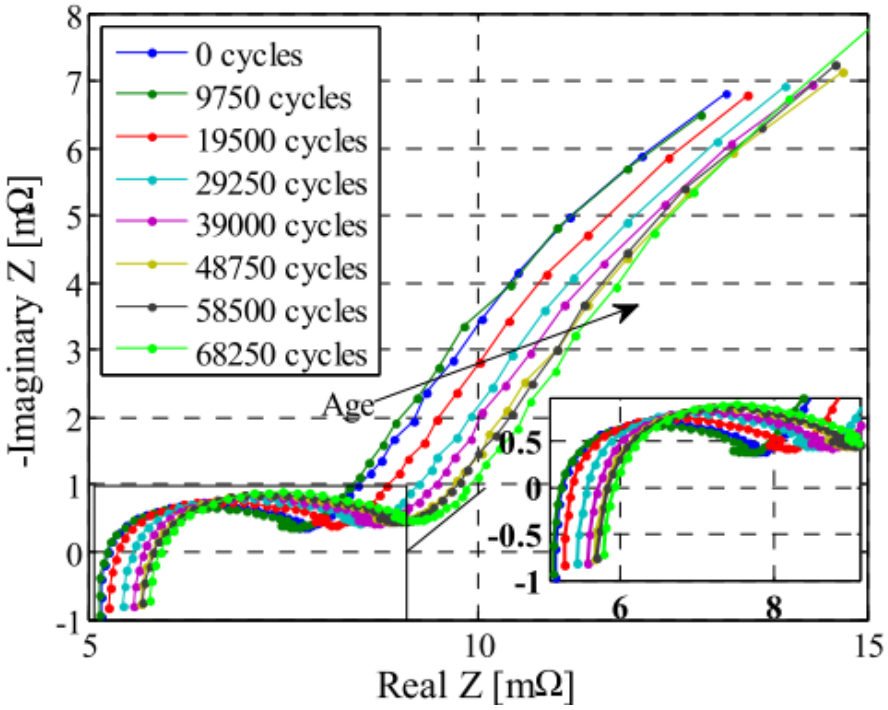

Figure 4.6 *Impedance dependency on battery cycle aging [4]*

In Fig. 4.6 the impedance on the far left is the impedance of the battery in BoL. The battery is then cycled 9750 times before the next impedance measurement and so on. In general, the trend in the battery impedance spectra during aging on cycling is that the impedance shifts towards right in the Nyquist plane. The main cause of the shifting is the increase of the battery ohmic resistance. Also, the semi-circle in higher frequencies grows, which corresponds to the charge transfer resistance growth.

In [4], model for the aging trend was made in terms of the ohmic resistance increase as function of number of cycles using a power function

$$R_{s,inc}[\%] = a_1 \cdot nc^{a_2}, \tag{4.7}$$

where a_1 is a coefficient of the power function, a_2 is the exponent of the power function and nc represents the number of cycles. While the previous aging dependency was measured during battery cycling, in Fig. 4.7 the battery aging is measured during various storage times.

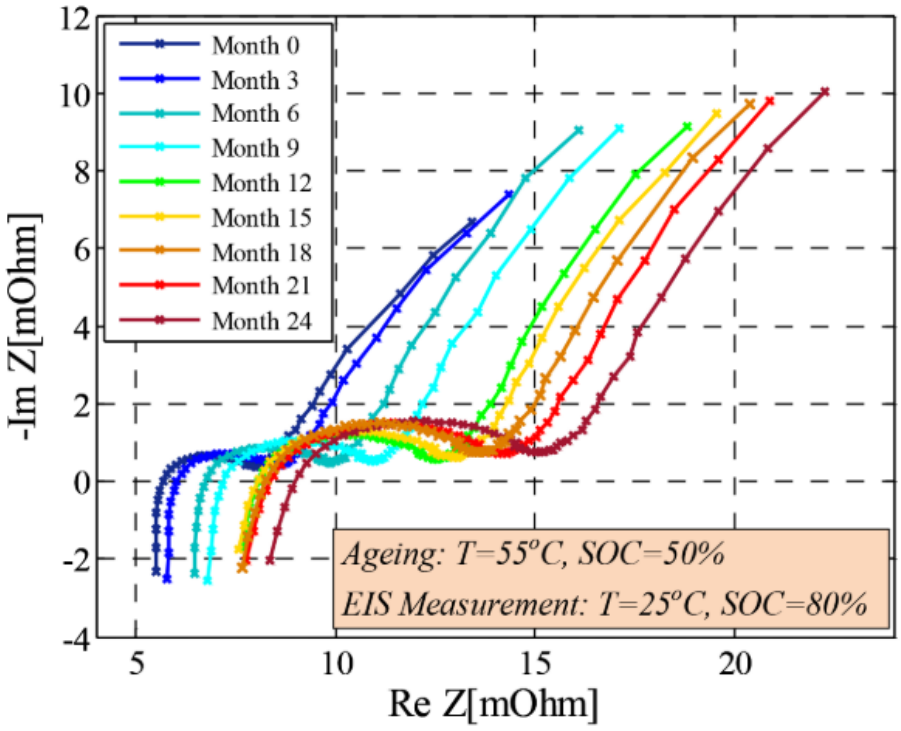

Figure 4.7 *Impedance dependency on battery storage aging [10]*

Same behavior in the battery impedance spectra can be seen in Fig. 4.7 than in the previous case. Increase of the ohmic resistance shifts the spectra to the right in the Nyquist plane. Internal resistance increase during battery storage time was discussed in [42] and the model for the increasing was described as

$$R_{s,inc}(t) = a_t \cdot t^{0.8}, \tag{4.8}$$

where $R_{s,inc}(t)$ represents resistance increase expressed as percentage, a_t is coefficient of the power law function and t is storage time in months. The coefficient a_t depends on the different cases studied in [42]. In the different aging cases, the battery SoC and storage temperature were changed. It was found that the ohmic resistance growth increases with higher temperature. Also, storing with higher SoC increased the ohmic resistance growth compared to lower SoC level.

5. POWER-HARDWARE-IN-THE-LOOP EMULATION OF BATTERY

Past studies have presented methods of battery emulation for hybrid vehicles (HEV) and electrical vehicles (EV) [18,20,58]. There is, however, a clear lack of studies that have focused on emulation methods for power systems. In this chapter, the PHIL setup of the battery emulation is described and the simulations and experimental results are presented.

5.1 Simulations

The Simulink model of the battery is presented in Fiq. 5.1

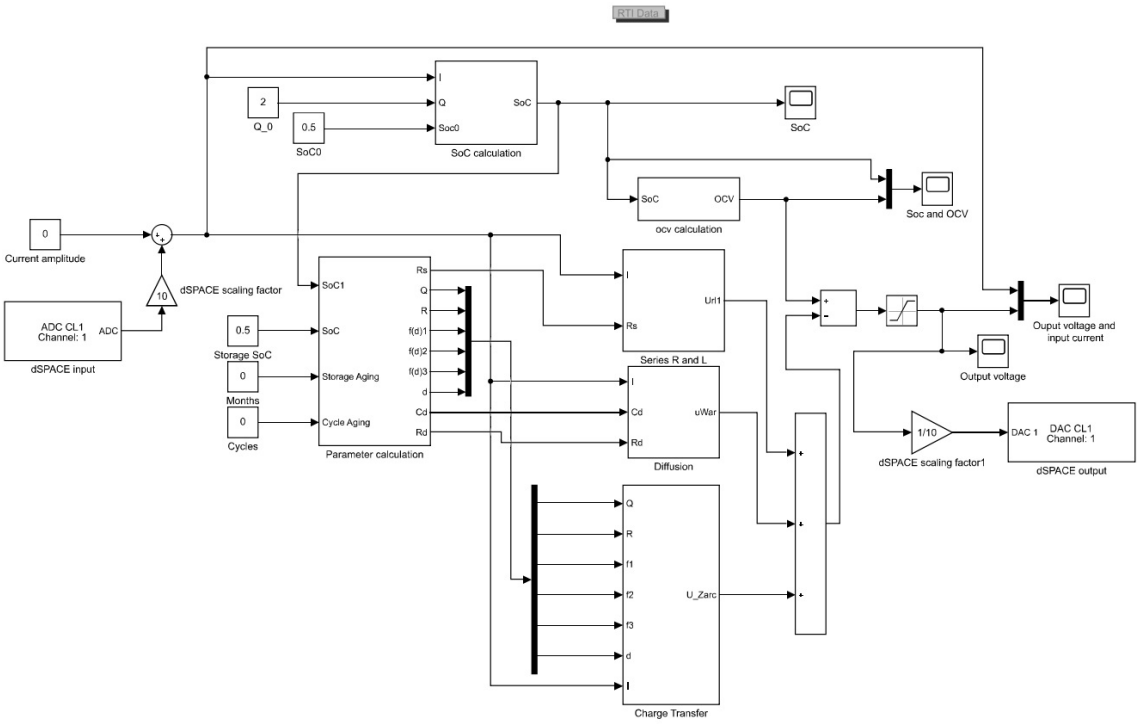

Figure 5.1 *Battery simulation model*

In the model, all the different impedance areas discussed earlier were modeled. The SoC was estimated using the Coloumb counting method and the OCV was modeled using Eq. 2.8. All the parameters for the impedance model were calculated in Matlab using a complex nonlinear least squares (CNLS) fitting algorithm. The algorithm was used for real measured impedance data of a Li-ion battery. An example of fitting can be seen in Fig. 5.2. The detailed Simulink model can be seen in Appendix A.

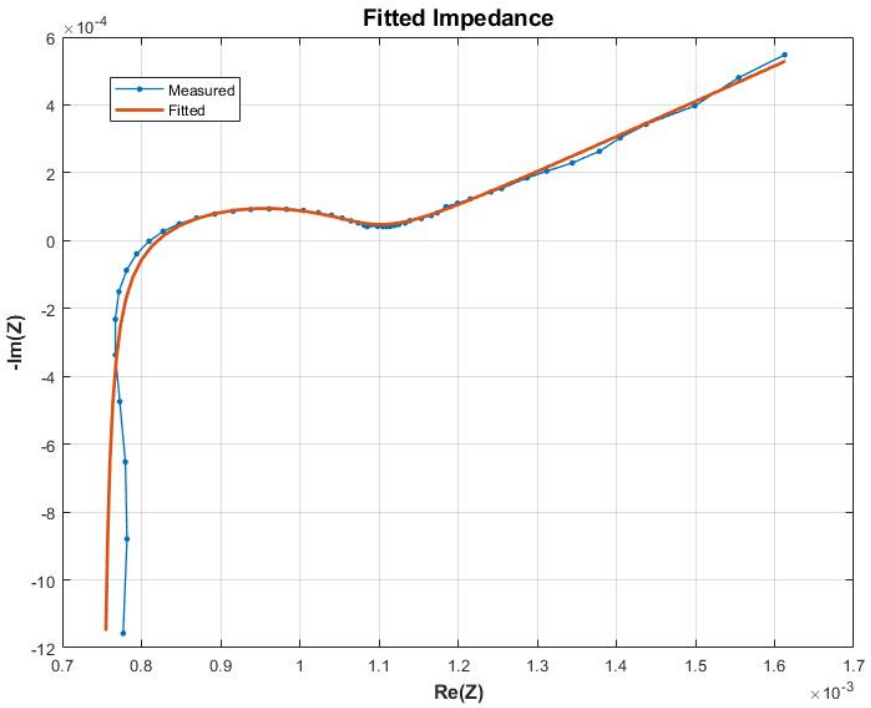

Figure 5.2 *Fitted impedance*

As seen in Fig. 5.2, the fitted impedance curve matches quite well with the real data. With this method, it is possible to extract the real battery impedance parameters. These parameters are used later in the emulation so that the emulator could act like a real battery. The fitted parameters extracted from the impedance curve in Fig. 5.2 are listed in Table 5.1

Table 5.1 *Fitted parameters for the battery impedance model*

Model parameters		
L_s	Series inductance	0.0186 μH
R_s	Series resistance	0.738 mΩ
R_{ct}	Charge transfer resistance	0.292 mΩ
R_d	Diffusion resistance	0.251 mΩ
C_{dl}	Double-layer capacitance	12.41 F
C_d	Diffusion capacitance	5732.12 F
d_1	Depression factor 1	0.78
d_2	Depression factor 2	0.52

5.2 Emulation setup

The battery emulation and measurement setup is shown in Fig. 5.3. The setup includes a 7 kW Spitzenberger Spies PVS 7000/BS simulator, dSPACE MicroLab-Box, National Instruments data acquisition unit USB-6363, PC wih ControlDesk real-time interface for controlling the battery current, a voltage probe and resistive load.

Figure 5.3 *Battery emulation setup*

The battery model was made in Simulink. The model was used alongside with dSPACE real-time interface and ControlDesk. The dSPACE compiles the Simulink model to a c-code and runs it continously, and the ControlDesk provides an interface in which the parameters of the model can be controlled in real-time. The data acquisition unit was used to generate the MLBS injection and measuring the output voltage of the emulator. Finally, the resistive load was used to discharge the amplified battery current.

Between the measurements, the battery storage aging and cycle aging was changed in Simulink, and the model was built again into the dSPACE. At first, the battery aging parameters was set to 0, so that the emulator would act like a new battery. The designed MLBS injection was used as an input in the battery model and the output

of the model was used as an input for the emulator voltage reference. The input excitation and the output response was measured using NI data acquisition unit. Next, the storage aging was changed to 12, 24 and 36 months, and the measurements were done in each condition.

The impedance dependency on the storage aging was modeled using Eq. 4.8 and Eq. 4.7. The battery storage SoC was set to 0.5 for all measurements.

The block diagram of the emulation setup is shown in Fig. 5.3

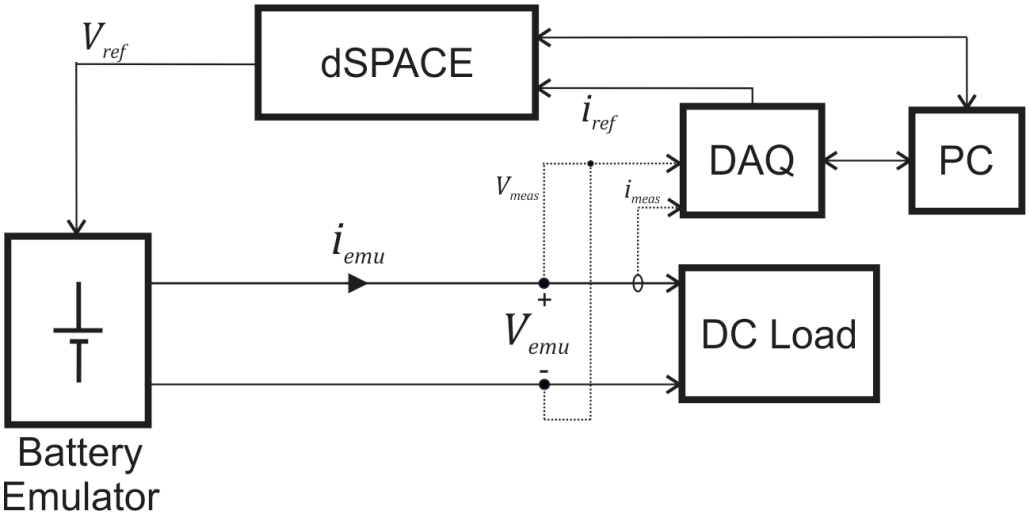

Figure 5.4 *Block diagram of the emulation setup*

5.3 Experimental results

The measurements were divided into high and low frequency areas and two MLBS injections were designed for these measurements. With only one injection, the results would not have been accurate enough in high or low frequency areas. The parameters for the MLBS injections used in the measurements are listed in Table 5.2. The emulated battery impedance measurement in Bode diagram with the reference impedance is shown in Fig. 5.5. The final results from the emulated battery storage aging and cycle aging are shown in Figures 5.6 and 5.7, respectively. Four different aging conditions were measured for both storage and cycle aging.

Table 5.2 *MLBS injection parameters used in the measurements*

	Low frequency MLBS	High frequency MLBS
Amplitude	10 A	10 A
f_{gen}	163.83 Hz	30 kHz
f_s	10 kHz	60 kHz
f_r	10 mHz	58.7 Hz
Frequency range	10 mHz-163.83 Hz	58.7 Hz - 6kHz
N	16 383	511
Averaging	2	30

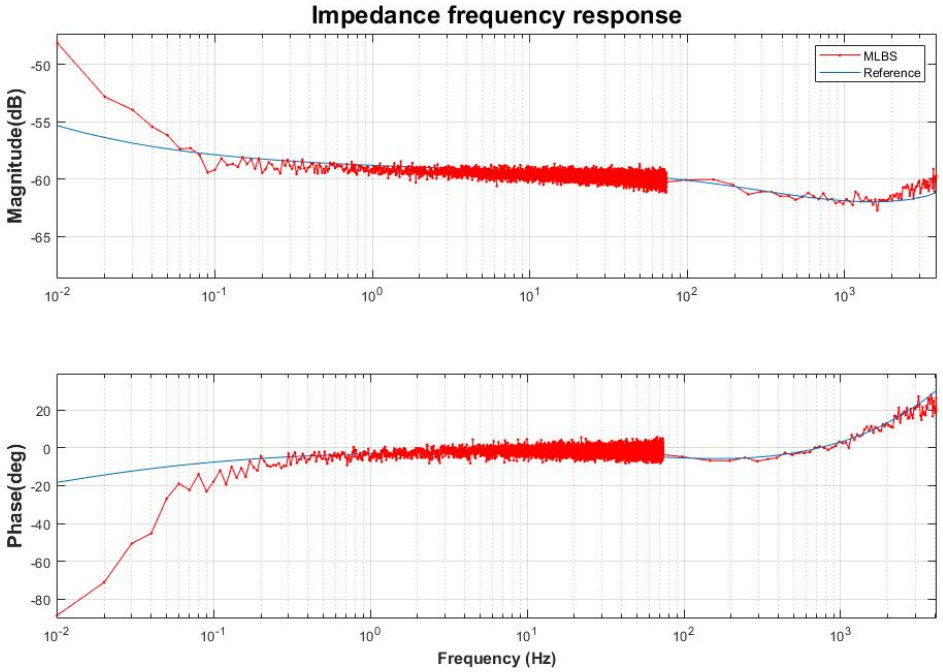

Figure 5.5 *Impedance frequency response measurement with reference*

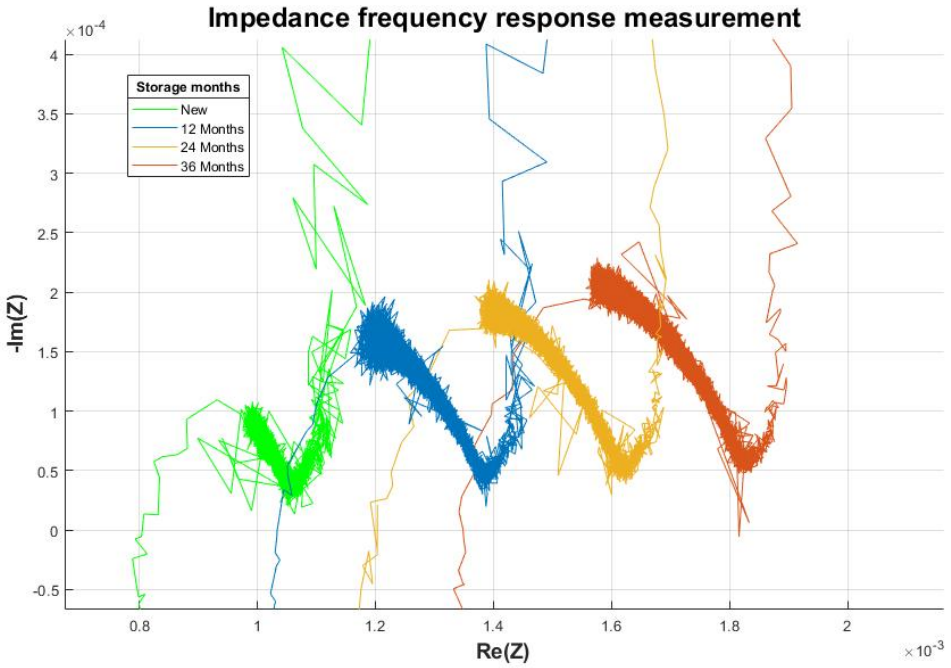

Figure 5.6 *Emulated battery impedance with different storage times*

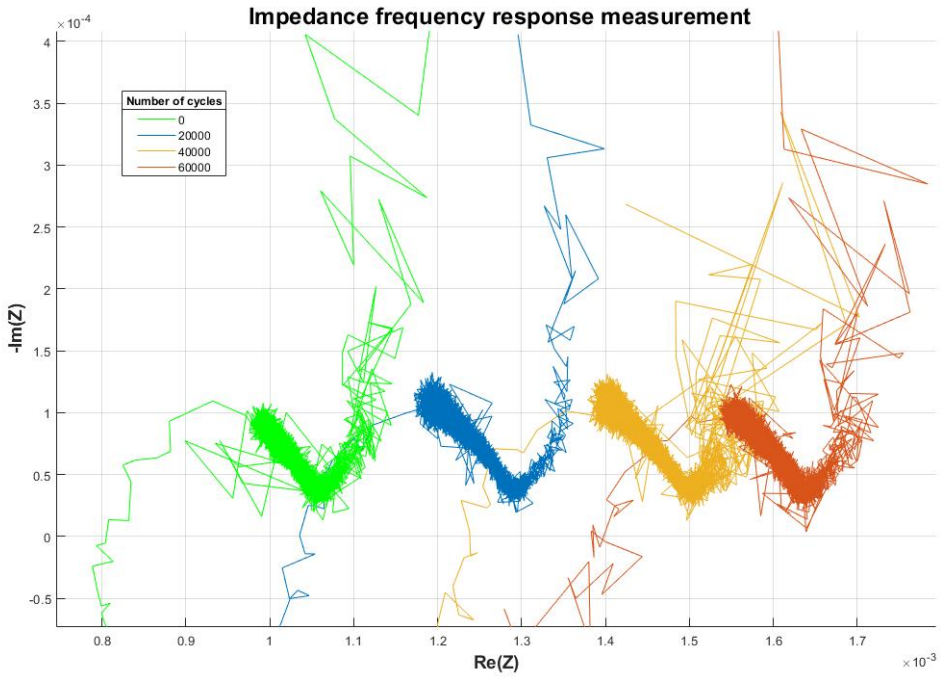

Figure 5.7 *Emulated battery impedance with different number of cycles*

Analysing the results

As seen from the Bode diagram in Fig. 5.5, the MLBS measurement is quite accurate from 0.5 Hz to 4 kHz. However, at the lower frequencies, that is, in the diffusion area, the phase angle starts to drop a lot faster than the reference. Furthermore, the magnitude also increases at the same frequencies more than the reference. The reference impedance is the same reference presented in Fig. 5.2 but transformed to Bode diagram. At first, this error was thought to be due to fact that the lower frequencies are simply harder to measure. However, it was found out that the reference impedance was modeled differently than the model in Simulink. As stated earlier, the approximations of the battery impedance model had to be made so that the model could even be constructed into Simulink. These approximations were not taken into account in the fitting procedure because the fitting was already really accurate with the ideal impedance models. Thus, some of the calculated model parameters were not matching the approximated models in Simulink. The approximated diffusion model shown in Fig. 3.10 acts quite differently especially at lower frequencies. This low frequency behavior can be seen in the aging measurements in Figures 5.6 and 5.7 as the curve starts to increase in the direction of imaginary axis.

Nevertheless, the measurements were done with these parameters because the diffusion area is not important when considering the aging phenomena. As seen from Fig. 5.6 the trend in the impedance spectrum is quite clear. The whole spectrum starts to shift towards right in the real axis and the semicircle in charge transfer area grows in both directions. This is due to fact that in the storage aging model the increase in the stored months affects to the all resistance parameters. These results correspond to the storage aging measurements made in [10] and shown in Fig. 4.7.

Furthermore, in the cycle aging measurements presented in Fig. 5.7 the whole impedance curve shift towards right and no other changes can be observed. This is because the cycle aging only affects the series resistance in the impedance model. It is noteworthy that the shifting is rapid at first but starts to decrease when more cycles are made.

6. CONCLUSION

The amount of lithium-ion batteries is rapidly increasing. This trend has set new challenges in battery analysis and recycling. As a consequence, the battery aging and performance deterioration have become one of the most studied issues in battery technology. The aging estimation is quite difficult because of the complex chemical reactions inside the battery. In addition, the aging mechanisms of the battery are slow and thus, analysing the battery aging is time-consuming.

This thesis has presented methods for modeling and measuring a Li-ion battery impedance and emulating the battery aging in real-time using a power hardware-in-the-loop method. First, a literature review of electrical energy storages was carried out with all the important theory and operation of a battery cell considering this work. The basic theory introduced the important concepts, such as the battery state of charge and the state of health.

The modeling of the Li-ion battery focuses on electrical equivalent models which were used to model the battery impedance. Additionally, the method for modeling the open-circuit voltage dependency of the battery state of charge was carried out. During the work, it was found out that the ideal impedance models could not be implemented in Simulink simulation environment. Thus, an approximated models of the battery impedance were also described. The impedance models were divided into different parts considering the different frequency areas where the chemical reactions occur. These areas are clearly visible in the complex plane representation of the battery impedance.

Wideband-identification methods based on maximum-length-binary-sequence (MLBS) injection and Fourier techniques were presented. In the methods, the MLBS is placed on top of the nominal battery current, and its response to the battery voltage is measured. Fourier methods are then applied to extract the spectral information of the impedance. The methods were shown to be well suited for fast battery-impedance measurements.

Experimental measurements were provided by using a power hardware-in-the-loop setup. Simulink model of the battery was compiled to c-code using a dSPACE real-time digital simulator. The dSPACE runs the model continuously and the model parameters can be changed in real time. The output of the dSPACE was used as a voltage reference for controlled voltage source with amplifier. MLBS injections were designed for two frequency areas of the battery impedance. The measurements were carried out by considering battery storage aging and cycle aging. The results verified that the emulation setup accurately models the aging of a lithium-ion battery.

It should be noted that the implemented aging model was only considering the aging of lithium iron phosphate type battery. In addition, the model only covered an impedance of a single battery cell. Real battery systems include many cells connected in series and parallel and their aging is independent. Further, the model did not consider the temperature of the stored batteries. The temperature has a great dependency on battery aging since it increases or decreases the speed of the reaction inside the battery. These are few improvements that should be considered in the modeling in order to get more realistic emulation setup.

BIBLIOGRAPHY

[1] B. Bose, "Global Energy Scenario and Impact of Power Electronics in 21St. Century," *IEEE Transactions on Industrial Electronics*, vol. 60, no. 7, pp. 2638–2651, 2013.

[2] Phil Weicker, *A Systems Approach to Lithium-Ion Battery Management*, 1st ed. Artech House, 2014.

[3] B. Scrosati and J. Garche, "Lithium batteries: Status, prospects and future," *Journal of Power Sources*, vol. 195, no. 9, pp. 2419–2430, 2010.

[4] D. I. Stroe, M. Swierczynski, A. I. Stan, V. Knap, R. Teodorescu, and S. J. Andreasen, "Diagnosis of lithium-ion batteries state-of-health based on electrochemical impedance spectroscopy technique," *2014 IEEE Energy Conversion Congress and Exposition (ECCE)*, pp. 4576–4582, 2014.

[5] Electric Power Research Institute, "Electricity Energy Storage Technology Options," *Power*, vol. 64, no. 2-3, p. 170, 2010.

[6] J. Sihvo, T. Messo, T. Roinila, and R. Luhtala, "Online Internal Impedance Measurements of Li-ion Battery Using PRBS Broadband Excitation and Fourier Techniques : Methods and Injection Design," in *International Power Electronics Conference*, 2018, pp. 2470–2475.

[7] E. Unamuno, L. Gorrotxategi, I. Aizpuru, U. Iraola, I. Fernandez, and I. Gil, "Li-ion battery modeling optimization based on Electrical Impedance Spectroscopy measurements," *2014 International Symposium on Power Electronics, Electrical Drives, Automation and Motion*, pp. 154–160, 2014.

[8] R.-E. Tudoroiu, M. Zaheeruddin, S.-m. Radu, and N. Tudoroiu, "Real-Time Implementation of an Extended Kalman Filter and a PI Observer for State Estimation of Rechargeable Li-Ion Batteries in Hybrid Electric Vehicle Applications-A Case Study," *Batteries*, vol. 4, no. 2, p. 19, 2018.

[9] J. Vetter, P. Novák, M. R. Wagner, C. Veit, K. C. Möller, J. O. Besenhard, M. Winter, M. Wohlfahrt-Mehrens, C. Vogler, and A. Hammouche, "Ageing mechanisms in lithium-ion batteries," *Journal of Power Sources*, vol. 147, no. 1-2, pp. 269–281, 2005.

[10] D.-i. Stroe, M. Swierczynski, A.-i. Stroe, and R. Teodorescu, "Lithium-ion battery power degradation modelling by electrochemical impedance spectroscopy," vol. 11, no. Oses 2016, pp. 1136–1141, 2017.

[11] J. Sihvo, "Internal impedance measurement techniques and charger dynamics for lithium-ion batteries," Master's thesis, Tampere University of Technology, 2017.

[12] C. Seitl, C. Messner, H. Popp, and J. Kathan, "Emulation of a High Voltage Home Storage Battery System using a Power Hardware-in-the-Loop Approach," *Proceedings of the Iecon 2016 - 42Nd Annual Conference of the Ieee Industrial Electronics Society*, pp. 6705–6710, 2016.

[13] J. D. Boles, Y. Ma, W. Cao, L. M. Tolbert, and F. Wang, "Battery Energy Storage Emulation in a Converter-Based Power System Emulator," *2017 Thirty Second Annual Ieee Applied Power Electronics Conference and Exposition (Apec)*, pp. 2355–2362, 2017.

[14] C. Seitl, J. Kathan, G. Lauss, and F. Lehfuss, "Selection and implementation of a generic battery model for PHIL applications," *IECON Proceedings (Industrial Electronics Conference)*, no. 1, pp. 5412–5417, 2013.

[15] ——, "Power hardware-in-The-loop implementation and verification of a real time capable battery model," *IEEE International Symposium on Industrial Electronics*, no. November, pp. 2285–2290, 2014.

[16] D. Abbes and A. Martinez, "Emulation of a hybrid PV-wind-battery system," *14th International Conference on Sciences and Techniques of Automatic Control and Computer Engineering, STA 2013*, pp. 443–447, 2013.

[17] A. Thanheiser, T. P. Kohler, C. Bertram, and H. G. Herzog, "Battery emulation considering thermal behavior," *2011 IEEE Vehicle Power and Propulsion Conference, VPPC 2011*, pp. 2–6, 2011.

[18] O. König, G. Gregorčič, and S. Jakubek, "Model predictive control of a DC-DC converter for battery emulation," *Control Engineering Practice*, vol. 21, no. 4, pp. 428–440, 2013.

[19] O. König, C. Hametner, G. Prochart, and S. Jakubek, "Battery emulation for power-HIL using local model networks and robust impedance control," *IEEE Transactions on Industrial Electronics*, vol. 61, no. 2, pp. 943–955, 2014.

[20] O. König, S. Jakubek, and G. Prochart, "Battery Impedance Emulation for Hybrid and Electric Powertrain Testing," pp. 62–67, 2012.

[21] R. M. Dell and D. A. J. Rand, *Understanding batteries*. Royal Society of Chemistry, 2001.

[22] T. Holm, "Litiumioniakuston Matalat Lämpötilat Huomioiva Impedanssimalli," Master's thesis, Tampere University of Technology, 2012.

[23] O. Tremblay, L. A. Dessaint, and A. I. Dekkiche, "A Generic Battery Model for the Dynamic Simulation of Hybrid Electric Vehicles," in *IEEE Vehicle Power and Propulsion Conf.*, 2007, pp. 284–289.

[24] G. L. Plett, "Extended Kalman filtering for battery management systems of LiPB-based HEV battery packs - Part 1. Background," *Journal of Power Sources*, vol. 134, no. 2, pp. 252–261, 2004.

[25] R. Xiong, J. Tian, H. Mu, and C. Wang, "A systematic model-based degradation behavior recognition and health monitoring method for lithium-ion batteries," *Applied Energy*, vol. 207, pp. 372–383, 2017.

[26] D. Linden and T. B. Reddy, *Linden's Handbook of Batteries*, 4th ed. McGraw-Hill's, 2011.

[27] H. Ishikawa, O. Mendoza, Y. Sone, and M. Umeda, "Study of thermal deterioration of lithium-ion secondary cell using an accelerated rate calorimeter (ARC) and AC impedance method," *Journal of Power Sources*, vol. 198, pp. 236–242, 2012.

[28] J. Sihvo, T. Roinila, and D. I. Stroe, "Online identification of internal impedance of Li-ion battery cell using ternary-sequence injection," no. September, pp. 2705–2711, 2018.

[29] J. Groot, "State-of-health estimation of Li-ion batteries: cycle life test methods," Ph.D. dissertation, Chalmers University of Technology, 2012.

[30] J. Li, E. Murphy, J. Winnick, and P. A. Kohl, "Studies on the cycle life of commercial lithium ion batteries during rapid charge-discharge cycling," *Journal of Power Sources*, vol. 102, no. 1-2, pp. 294–301, 2001.

[31] R. Hausbrand, G. Cherkashinin, H. Ehrenberg, M. Gröting, K. Albe, C. Hess, and W. Jaegermann, "Fundamental degradation mechanisms of layered oxide Li-ion battery cathode materials: Methodology, insights and novel approaches," *Materials Science and Engineering B: Solid-State Materials for Advanced Technology*, vol. 192, no. C, pp. 3–25, 2015.

[32] J.-K. Park, *Principles and Applications of Lithium Secondary Batteries*, 1st ed. Wiley-VCH, 2012.

[33] L. Vinet and A. Zhedanov, *Lithium Batteries*, nov 2010, vol. 53, no. 9.

[34] R. Al Nazer, V. Cattin, P. Granjon, M. Montaru, and M. Ranieri, "Broadband identification of battery electrical impedance for HEVs," *IEEE Transactions on Vehicular Technology*, vol. 62, no. 7, pp. 2896–2905, 2013.

[35] A. R. Sparacino, G. F. Reed, R. J. Kerestes, B. M. Grainger, and Z. T. Smith, "Survey of battery energy storage systems and modeling techniques," *2012 IEEE Power and Energy Society General Meeting*, pp. 1–8, 2012.

[36] Camry Instruments, "Basics of Electrochemical Impedance Spectroscopy," 2010.

[37] S. Buller, M. Thele, R. D. Doncker, and E. Karden, "Impedance-Based Simulation Models of Supercapacitors and Lithium-ion Batteries for Power Electronic Applications," *IEEE Industry Applications Magazine*, vol. 11, no. 2, pp. 742–747, 2005.

[38] E. Karden, "Using low-frequency impedance spectroscopy for characterization, monitoring, and modeling," Ph.D. dissertation, RWTH Aachen, 2002.

[39] A. Ramamurthy, S. Notani, and S. Bhattacharya, "Advanced lithium ion battery modeling and power stage integration technique," *2010 IEEE Energy Conversion Congress and Exposition, ECCE 2010 - Proceedings*, pp. 1485–1492, 2010.

[40] D. Andre, M. Meiler, K. Steiner, H. Walz, T. Soczka-Guth, and D. U. Sauer, "Characterization of high-power lithium-ion batteries by electrochemical impedance spectroscopy. II: Modelling," *Journal of Power Sources*, vol. 196, no. 12, pp. 5349–5356, 2011.

[41] S. Buller, "Impedance-Based Simulation Models for Energy Storage Devices in Advanced Automotive Power Systems," PhD. Dissertation, Aachen University of Technology, Aachen, 2003.

[42] D. I. Stroe, M. Swierczynski, S. K. Kær, and R. Teodorescu, "Degradation Behavior of Lithium-Ion Batteries During Calendar Ageing - The Case of the Internal Resistance Increase," *IEEE Transactions on Industry Applications*, vol. 54, no. 1, pp. 517–525, 2018.

[43] A. Barré, B. Deguilhem, S. Grolleau, M. Gérard, F. Suard, and D. Riu, "A review on lithium-ion battery ageing mechanisms and estimations for automotive applications," *Journal of Power Sources*, vol. 241, pp. 680–689, 2013.

[44] L. Z. Wang, L. J. Ning, S. B. Fang, Y. P. Wu, and R. Holze, "Carbon anode materials from polysiloxanes for lithium ion batteries," *Journal of Solid State Electrochemistry*, vol. 9, no. 7, pp. 520–523, 2004.

[45] E. Peled, "The Electrochemical Behavior of Alkali and Alkaline Earth Metals in Nonaqueous Battery Systems-The Solid Electrolyte Interphase Model," *Electrochem. Soc.*, vol. 126, no. 12, pp. 2047–2051, 1979.

[46] H. Buqa, A. Würsig, J. Vetter, M. E. Spahr, F. Krumeich, and P. Novák, "SEI film formation on highly crystalline graphitic materials in lithium-ion batteries," *Journal of Power Sources*, vol. 153, no. 2, pp. 385–390, 2006.

[47] U. Tröltzsch, O. Kanoun, and H. R. Tränkler, "Characterizing aging effects of lithium ion batteries by impedance spectroscopy," *Electrochimica Acta*, vol. 51, no. 8-9, pp. 1664–1672, 2006.

[48] J. Schoukens, K. Godfrey, and M. Schoukens, "Nonparametric Data-Driven Modeling of Linear Systems: Estimating the Frequency Response and Impulse Response Function," *IEEE Control Systems*, vol. 38, no. 4, pp. 49–88, 2018.

[49] T. Roinila, "Fast frequency response measurement techniques in analyzing the dynamics of switched-mode power supplies," Ph.D. dissertation, Tampere University of Technology, 2010.

[50] K. Godfrey, "Design and application of multifrequency signals," *Computing and Control Engineering Journal*, vol. 2, no. 4, pp. 187–195, 1991.

[51] A. H. Tan and K. R. Godfrey, "The generation of binary and near-binary pseudorandom signals: An overview," *IEEE Transactions on Instrumentation and Measurement*, vol. 51, no. 4, pp. 583–588, 2002.

[52] T. Roinila and T. Messo, "Online Grid-Impedance Measurement Using Ternary-Sequence Injection," *IEEE Transactions on Industry Applications*, vol. 54, no. 5, pp. 5097–5103, 2018.

[53] W. Waag, S. Käbitz, and D. U. Sauer, "Experimental investigation of the lithium-ion battery impedance characteristic at various conditions and aging states and its influence on the application," *Applied Energy*, vol. 102, pp. 885–897, 2013.

[54] H. Dai, B. Jiang, and X. Wei, "Impedance Characterization and Modeling of Lithium-Ion Batteries Considering the Internal Temperature Gradient," *Energies*, vol. 11, no. 1, p. 220, 2018.

[55] U. Tröltzsch, O. Kanoun, and H. R. Tränkler, "Characterizing aging effects of lithium ion batteries by impedance spectroscopy," *Electrochimica Acta*, vol. 51, no. 8-9, pp. 1664–1672, 2006.

[56] M. Galeotti, L. Cinà, C. Giammanco, S. Cordiner, and A. Di Carlo, "Performance analysis and SOH (state of health) evaluation of lithium polymer batteries through electrochemical impedance spectroscopy," *Energy*, vol. 89, pp. 678–686, 2015.

[57] J. Jiang, Z. Lin, Q. Ju, Z. Ma, C. Zheng, and Z. Wang, "Electrochemical Impedance Spectra for Lithium-ion Battery Ageing Considering the Rate of Discharge Ability," *Energy Procedia*, vol. 105, pp. 844–849, 2017.

[58] O. König, C. Hametner, G. Prochart, and S. Jakubek, "Battery emulation for power-HIL using local model networks and robust impedance control," *IEEE Transactions on Industrial Electronics*, vol. 61, no. 2, pp. 943–955, 2014.

APPENDIX A: SIMULINK MODELS

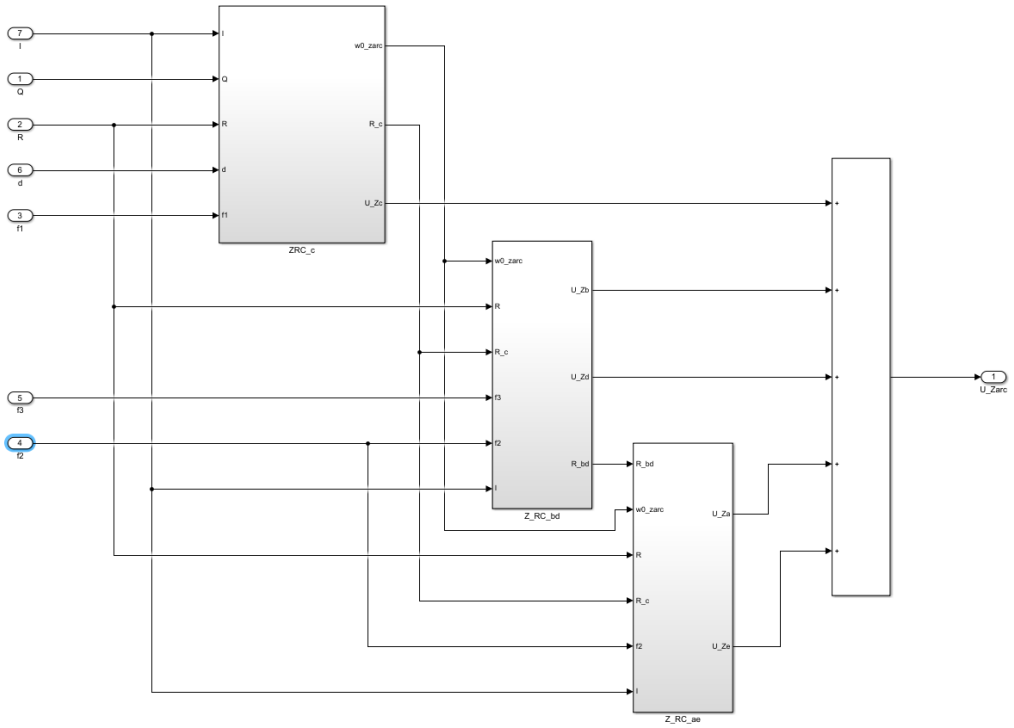

Figure 1 *Simulink model of ZARC element*

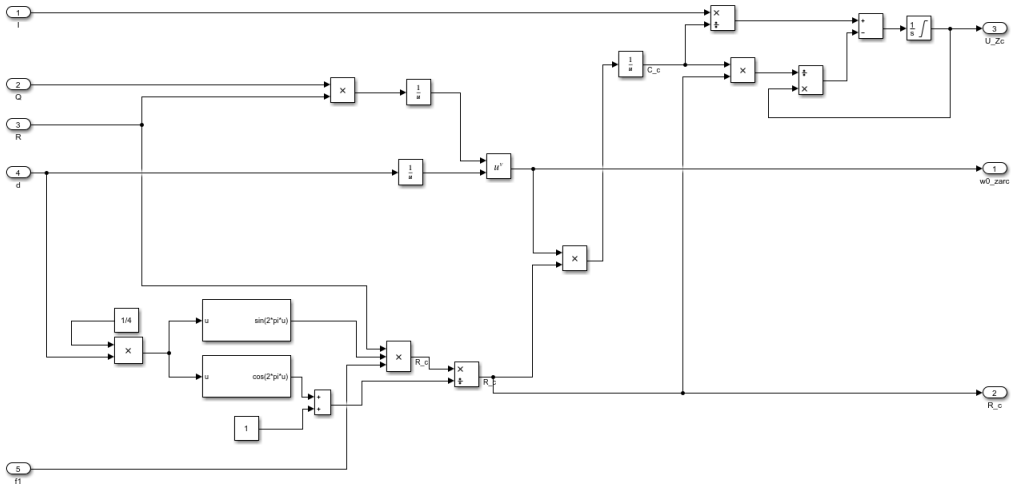

Figure 2 *Simulink model of the middle approximated ZARC element*

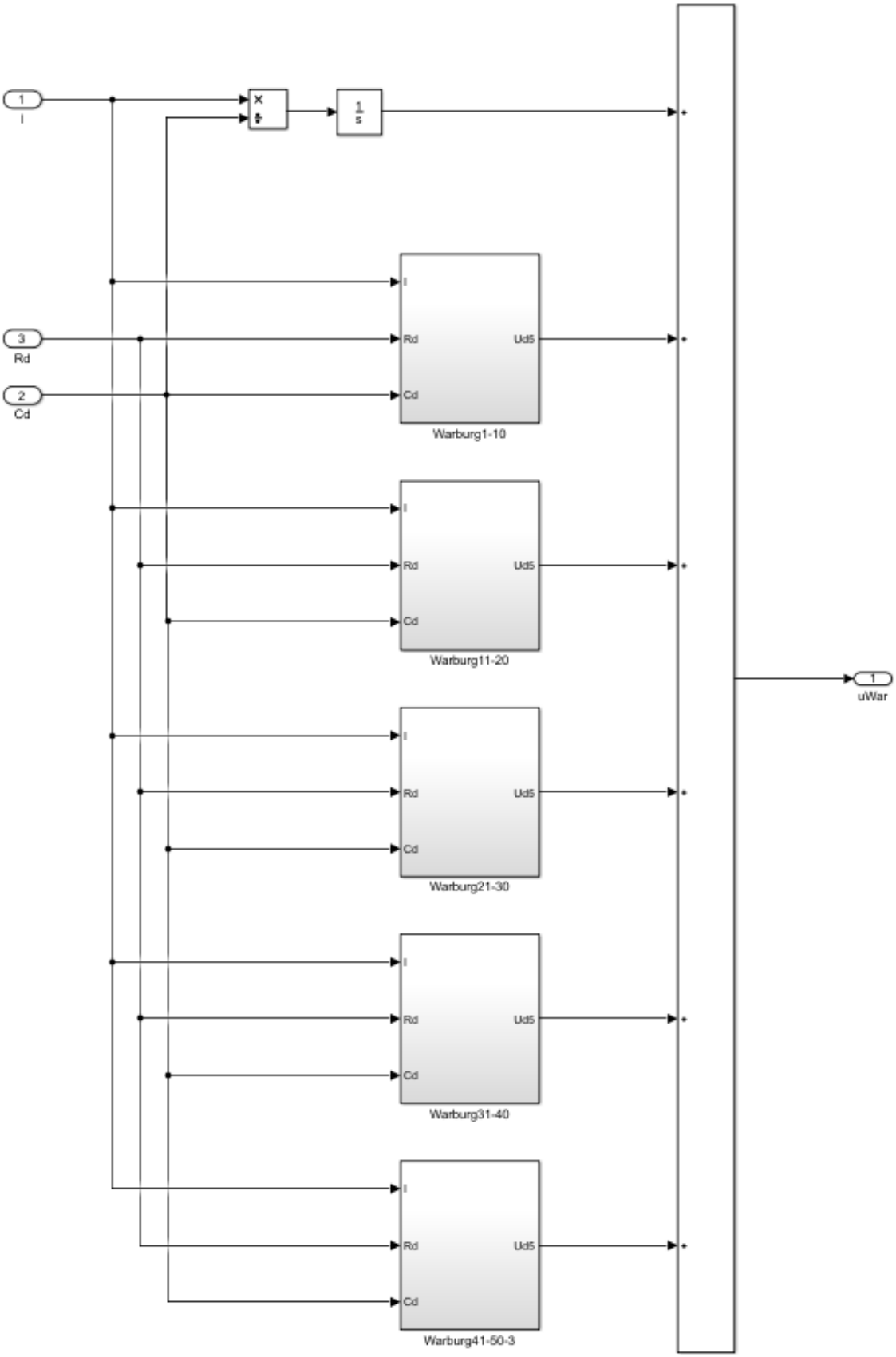

Figure 3 *Simulink model of Warburg impedance*

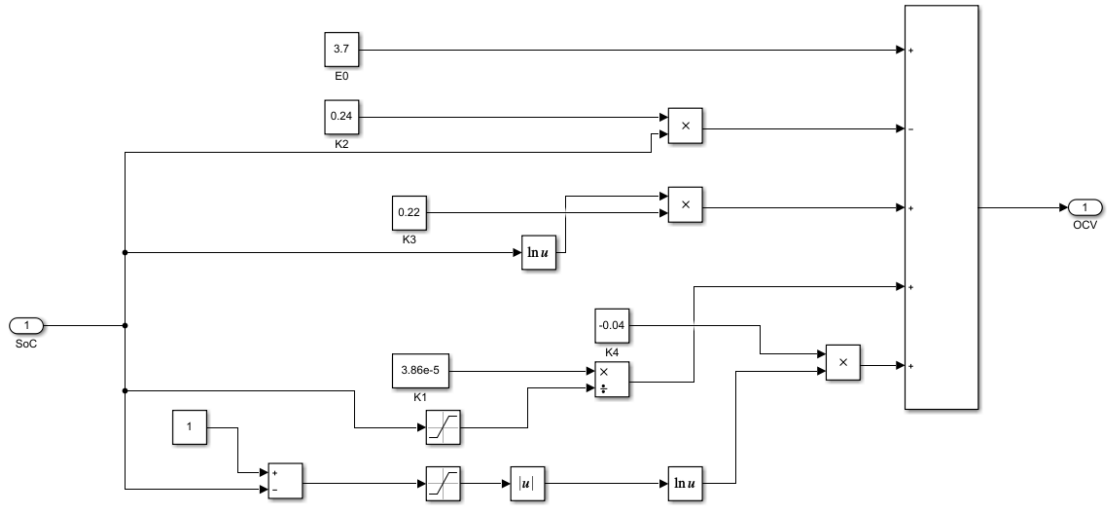

Figure 4 *Open-circuit voltage calculation model*